THE FLORIDA STATE UNIVERSITY

COLLEGE OF ENGINEERING

Analysis, Modeling and Simulation of Optimal Power Tracking of Multiple-Modules of Paralleled Solar Cell Systems

By

Adedamola Omole

A Thesis submitted to the
Department of Electrical Engineering
in partial fulfillment of the
requirements for the degree of
Master of Science

Degree Awarded:
Fall Semester, 2006

The members of the Committee approve the thesis of Adedamola Omole defended on 07/18/2006.

Jie J. Chang
Professor Directing Thesis

Simon Y. Foo
Committee Member

Rodney G. Roberts
Committee Member

Approved:

L. J. Tung, Interim Chair, Department of Electrical and Computer Engineering

C. J. Chen, Dean, College of Engineering

The Office of Graduate Studies has verified and approved the above named committee members.

ACKNOWLEDGMENTS

I would like to take this opportunity to thank my supervisor Dr. Jie Chang for his valuable guidance and support throughout my graduate program. I would like to thank my committee members, Dr. Simon Foo and Dr. Rodney Roberts, for their generous advice and interest.

I would also like to thank the academic and administrative staff in the Department of Electrical and Computer Engineering and the Center for Advanced Power Systems (CAPS).

Finally, I would like to thank my family and friends for their support throughout my graduate school experience.

TABLE OF CONTENTS

LIST OF FIGURES

LIST OF TABLES

ABSTRACT

Distributed and renewable energy generation (DG) offers great potential in meeting future global energy requirements. Distributed generation consists of small to medium size generators cited close to the customer and spread across a power system. The production of power from renewable energies will lead to a significant reduction in the rate of environmental pollution in comparison with the production by fossil fuels, thus gaining renewed attention due to advances in technology, environmental concerns and a growing energy demand. Photovoltaic systems in particular have great potential when compared to other renewable energies. The goals of this thesis are to perform a systematic analysis, modeling and evaluation of the key subsystems or components of a multiple-source renewable energy generation system and to develop an optimal tracking and control strategy. It is desirable to achieve maximum power output at a minimum cost under various operating conditions.

CHAPTER 1

Introduction

1.1 Objectives

The main challenge in replacing legacy systems with newer more environmentally friendly alternatives is how to capture the maximum energy and deliver the maximum power at a minimum cost for a given load. A combination of two or more types of energy sources might offer the best chance of optimizing power generation by varying the contribution from each energy source depending on the load demand. The goal is to develop and optimize maximum power tracking and control of a future Multi-Source Renewable Distributed Energy Generation (MRDEG) system.

At a subsystem level, solar power is a renewable energy source that might one day soon replace fossil fuel dependent energy sources. However, for that to happen, solar power cost per kilowatt-hour has to be competitive with fossil fuel energy sources. Currently, solar panels are not very efficient with only about 12 ~ 20% efficiency in their ability to convert sunlight to electrical power. The efficiency can drop further due to other factors such as solar panel temperature and load conditions. In order to maximize the power derived from the solar panel it is important to operate the panel at its optimal power point. To achieve this, a type of charge controller called a Maximum Power Point Tracker will be designed and implemented.

A solar cell is a non-linear power source and its output power depends on the terminal operating voltage. The Maximum Power Point Tracker (MPPT) compensates for the varying voltage vs. current characteristics of the solar cell. The MPPT tracks the output voltage and current from the solar cell and determines the operating point that will deliver the most power. The proposed MPPT must be able to accurately track the constantly-varying operating point where the maximum power is delivered in order to increase the efficiency of the solar cell.

1.2 Motivation

The finite global supply of recoverable fossil fuels implies that at some point in the future, alternative sources of energy will become the primary source of energy to meet global demand. Solar and fuel cells represent promising alternatives that will likely initially supplement fossil fuel based energy supply, and eventually replace the fossil fuel energy sources as the availability of the latter declines. There is therefore a need to systematically analyze and understand how solar and fuel cells operate together as an optimal system.

When compared to fossil fuels, solar and fuel cells are relatively untapped sources of energy, thus there still remains a lot of work to be done to make solar and fuel cells as efficient and reliable as possible. One approach to understanding and improving solar and fuel cell efficiency is digital modeling and simulation. After successfully modeling and simulating solar and fuel cells, it is possible to develop methods to optimizing the system operation. The main objective of this research is to first model and simulate the solar cell subsystem, then optimize the combined system operation based on both solar and fuel cells to make it as efficient as possible, with a focus on the given solar subsystem.

1.3 Technology Overview

The primary source of fuel for a majority of current power systems are fossil fuels such as crude oil and coal. These non-renewable forms of energy on earth are ultimately finite sources of energy. Also burning of oil and coal in the process of conversion to electrical power can be quite harmful to the environment. Over the past decades there has been a lot of interest in alternative sources of energy and several approaches have been suggested to replacing existing energy sources. Renewable energy sources like solar and wind have shown promise as possible cost efficient alternatives to fossil fuels.

As the world energy supplies continue to tighten due to rapid global economic growth, the scramble for limited available energy resources is fueling a rapid increase in the price of crude oil and natural gas, the primary sources of energy around the world. The growth in demand and the attendant increase in price have promoted the development of alternative energy technologies. Distributed power generation based on renewable energy is one of such alternative methods. These alternative energy technologies are now being deployed to meet the world energy demand.

The bulk of electric power used in the world today comes from large central station power plants, most of which utilize fossil fuel combustion to produce steam for driving steam turbine generators. The existing large central generating units are not very efficient as they covert less than 40% of the energy in their fuel to useful electric power [1]. In comparison, small fuel cells and microturbines suitable for distributed generation have been shown to have efficiency up to 40% [1]. While these higher efficiency claims are not irrefutable, there seems to be little doubt that modern distributed generation units can achieve efficiencies equal to or better than existing central station power plants.

The distributed power generation includes the application of small to medium size generators, generally less than 15MW, scattered across a power system to supply electrical power needed by customers. When generating stations are located far away from the consumer, power has to be transmitted over long distances and there are significant amounts of power losses as a result of transmission and distribution. By locating generating stations close to consumers, distributed generation provides advantages in efficiency and flexibility over traditional large-scale, capital-intensive central-station power plants.

1.4 Thesis Organization

The thesis consists of six chapters, with the first chapter highlighting current opportunities and challenges to renewable energy generation and distribution. The motivation for conducting this research is discussed as well as the expected outcome. The first chapter also gives an overview of some current technologies and compares the possible advantages of one technology over the other.

Chapter 2 will provide a description of the proposed system and review the components of the system. It will include a literature review on the photovoltaic subsystem, the solar cell characteristics and cell operation. Charge application and MPPT controllers will also be reviewed while the selected fuel cells and energy storage devices will be discussed.

Chapter 3 will focus on the analysis and modeling of the system and subsystems. Mathematical and circuit models of the system will be established based on optimal system architecture. The solar module will be modeled and simulated in PSpice. The MPPT requirement will be determined and a design proposed.

Chapter 4 will include the discussion of the practical circuit elements and the testing and verification of the MPPT model. Here the photovoltaic (PV) model will be validated using the manufacturer supplied data. This chapter will also present some experimental data which will be used confirm the theory on solar cell properties.

In chapter 5, the MPPT circuit model and operation will be validated. Control and optimization methods for the MPPT will be highlighted. The use of microcontrollers and artificial neural networks in controlling the MPPT operation will also be discussed. The final chapter concludes the thesis with a look on the future development of this work. The references and appendix will be attached at the end of the thesis.

CHAPTER 2

Multi-Source Renewable Distributed Energy Generation

2.1 Block Diagram of New MRDEG System

For the future Multi-Source Renewable Distributed Energy Generation system being considered, multiple solar power subsystems based on photovoltaic cell (PVC) arrays will be operated in parallel connection with fuel-cell arrays and high-density energy storage components, including super-capacitors. A block diagram of the proposed MRDEG system is shown in Fig 2.1. In order to achieve maximum energy capture and maximum power output, the photovoltaic cells should be operated at certain optimal operating points. The overall power captured by the PVC panels, and the DC or AC output power is a function of the system's operating points such as the voltages and currents of different incoming sources to the energy storage capacitors.

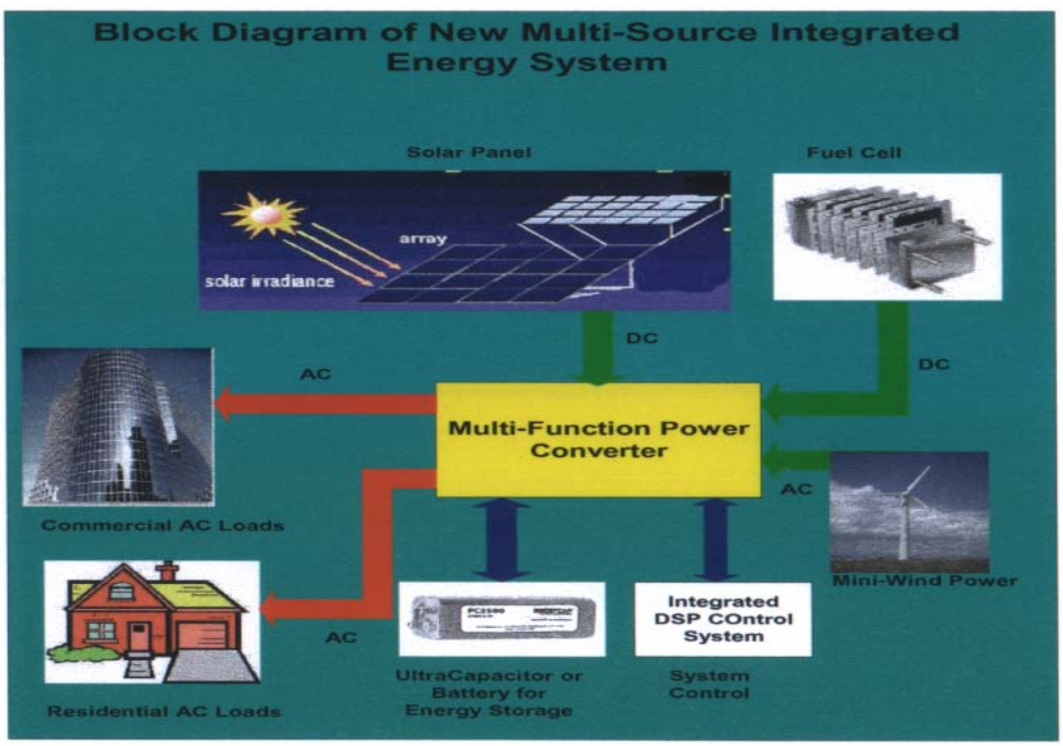

Fig 2.1: Block diagram of proposed MRDEG system

2.2 Photovoltaic Subsystem

A photovoltaic (PV) system consists of solar panels that generate electricity by the direct conversion of the sun's energy into electricity. The solar panels consist mainly of semiconductor material, with Silicon being the most commonly used. The components of a PV system are the solar cells connected in a suitable form and the electronic devices that interface the storage elements and the AC or DC loads.

One of the major tasks in controlling photovoltaic cells for power generation is improving cell efficiency and maximizing energy extraction. This requires I-V (current-to-voltage) measurements to characterize performance and determine the load impedance that best matches the cell's source impedance. The best match can then be determined on a point on the I-V curve of the solar cell.

2.2.1 Solar Cell Characteristics

Solar cells consist of a p-n junction fabricated in a thin layer of semiconductor. The semiconductor electros can be located in either the valence band or conduction band. Initially, all the electrons in the semiconductor fill up the valence band but when sunlight hits the semiconductor, some electrons acquire enough energy to move from the valence band to the conduction band [2]. The electrons in the conduction band then begin to move freely creating electricity. The electron leaving the valence band leaves a positively charged hole behind and now that the valence band is no longer full, it aids the current flow. Most solar cells are doped to reduce the energy required for the electron to move from the valence band to the conduction band [3].

The amount of energy from sunlight, called photons, that is absorbed by a solar cell determines its efficiency. A photon can be reflected, absorbed or it can pass through a semiconductor [4]. Since only the photons that are absorbed contribute to the electrical energy, it is important to reduce the percentage of photons that pass through and that are reflected. An anti-reflective coating is usually applied to the surface of the solar cell to decrease the number of photons that are reflected. This reduces the percentage of photons that are reflected but some photons are still able to pass right through the semiconductor material.

The photons in sunlight have a wide range of wavelengths, and some photons at certain wavelengths are able to pass through the semiconductor material. If a photon has energy lower than the band gap energy of the semiconductor, the photon is unable to create an electron-hole pair and the semiconductor will not absorb the photon [4]. On the other hand, if a photon has more energy than the band gap of the semiconductor, the photon is absorbed by the valence band electron and any excess energy is emitted as a form of heat while the electron settles down in the conduction band. To reduce the percentage of photons that pass through, some semiconductors are manufactured with several layers, each having a different band gap to maximize the amount of photons that are absorbed.

There are several approaches to manufacturing solar cells, including the kind of semiconductor used and the crystal structure employed, with each different factor affecting the efficiency and cost of the cell. Other external factors such as the ambient weather conditions like temperature, illumination, shading, etc also affect the solar panel's output. The aim is to design a system that will extract the most possible power regardless of ambient weather conditions or solar cell efficiency.

2.2.2 Solar I-V Characteristics

The current-to-voltage characteristic of a solar cell is non-linear, which makes it difficult to determine the maximum power point. It is straightforward to determine the maximum power point on a linear curve as maximum power is transferred at the midpoint of the current-voltage characteristic. A typical I-V characteristic of a solar cell is shown in Fig. 2.2.

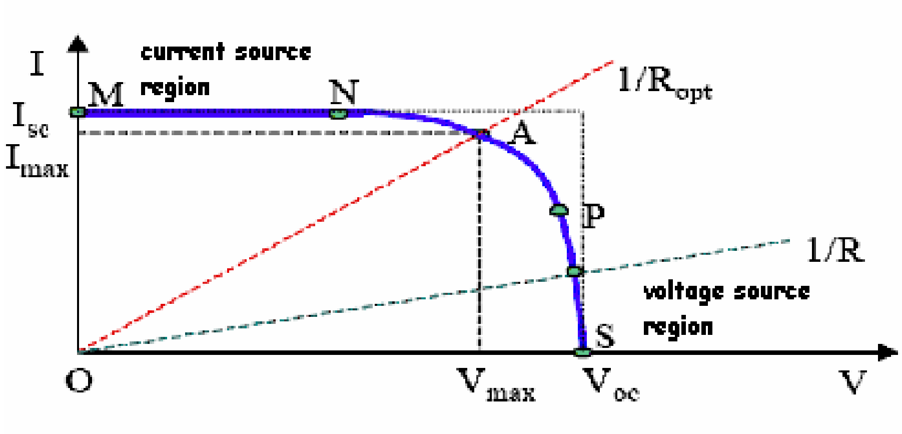

Fig 2.2: Typical I-V characteristic of a solar cell in steady-state operation

For a solar cell, the non-linear relationship means the maximum power point has to be determined by calculating the product of the voltage and output current. In order to extract maximum power from the solar cell, the solar cell must always be operated at or very close to where the product of the voltage and output current is the highest. This point is referred to as the maximum power point (MPP), and it is located around the 'bend' or 'knee' of the I-V characteristic.

The operating characteristic of a solar cell consists of two regions: the current source region, and the voltage source region. In the current source region, the internal impedance of the solar cell is high and this region is located on the left side of the current-voltage curve. The voltage source region, where the internal impedance is low, is located on the right side of the current-voltage curve. As can be observed from the characteristic curve, in the current source region, the output current remains almost constant as the terminal voltage changes and in the voltage source region, the terminal voltage varies only minimally over a wide range of output current.

According to the maximum power transfer theory, the power delivered to the load is maximum when the source internal impedance matches the load impedance [5]. For the system to operate at or close to the MPP of the solar panel, the impedance seen from the input of the MPPT needs to match the internal impedance of the solar panel. Since the impedance seen by the MPPT is a function of voltage (V = I * R), the main function of the MPPT is to adjust the solar panel output voltage to a value at which the panel supplies the maximum energy to the load. However, maintaining the operating point at the maximum power point can be quite challenging as constantly changing ambient conditions such as irradiance and temperature will vary the maximum operating point. Hence, there is a need to constantly track the power curve and keep the solar panel operating voltage at the point where the most power is extracted.

Irradiance is a characteristic related to the amount of sun energy reaching the ground, and under ideal conditions it is measured as 1000 W/m^2 at the equator. The sun energy around the earth is highest around the equator when the sun is directly overhead. Some important magnitudes related to irradiance include the spectral irradiance, irradiance, and radiation. Spectral irradiance is the power received by a unit surface area at a particular wavelength, while irradiance is the integral of the spectral irradiance extended to all wavelengths of interest. Radiation is the time integral of the irradiance extended over a given period of time.

In designing PV systems, the main concern is the radiation received from the sun at a particular location at a given inclination angle and orientation and for long periods of time. Since solar radiation is the energy resource of the solar panel, the output of the panel is significantly affected by changing irradiance. The I-V characteristic of a solar cell including the effects of irradiance is shown in Fig. 2.3.

The irradiance at any location is strongly dependent on the orientation and inclination angles of the solar panel. Orientation is usually measured relative to the south in northern latitudes while it is measured relative to the north in southern latitudes. On the other hand, the inclination angle is measured relative to the horizontal. Using these two parameters, the irradiation at any location can be determined. The irradiance information for many sites worldwide is widely available on the internet.

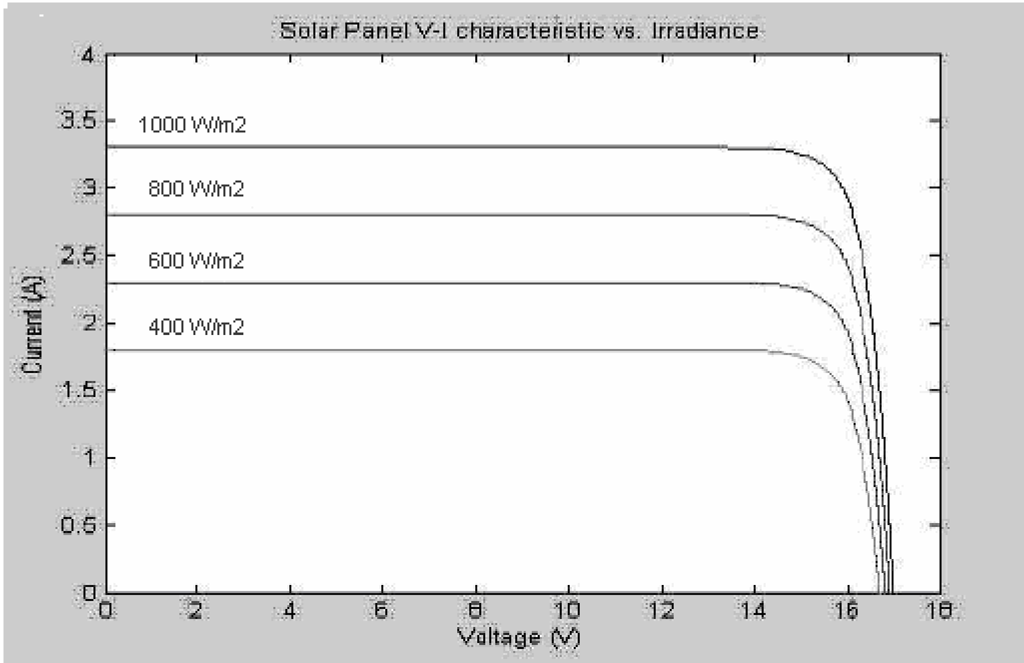

Fig 2.3: Typical solar cell I-V characteristic showing effect of irradiance

As can be observed from Fig. 2.3, the output power is directly proportional to the irradiance. As such, a smaller irradiance will result in reduced power output from the solar panel. However, it is also observed that only the output current is affected by the irradiance. This makes sense since by the principle of operation of the solar cell the generated current is proportional to the flux of photons. When the irradiance or light intensity is low, the flux of photon is less than when the sun is bright and the light intensity is high, thus more current is generated as the light intensity increases. The change in voltage is minimal with varying irradiance and for most practical application, the change is considered negligible.

Although irradiance is an important factor in determining the I-V characteristic of a solar panel, it is not the only factor. Temperature also plays an important role in predicting the I-V characteristic, and the effects of both factors have to be considered when designing a PV system. Whereas the irradiance mainly affects the output current, the temperature mainly affects the terminal voltage. A plot of I-V characteristic with varying temperature is shown below.

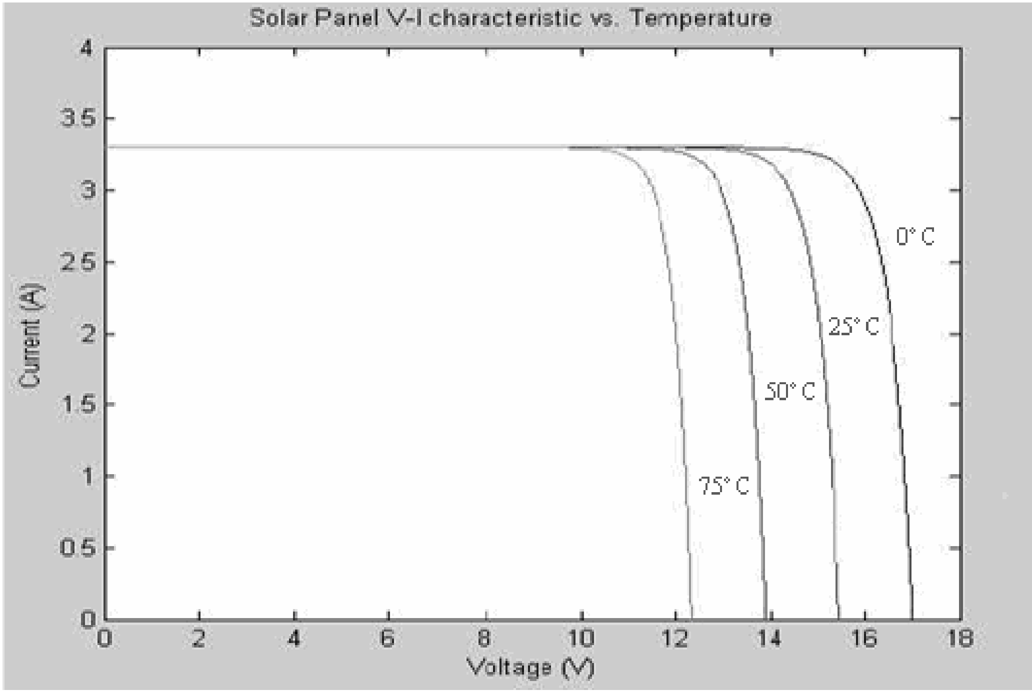

Fig 2.4: Typical solar cell I-V characteristic showing effect of temperature

It is observed from Fig. 2.4 that the terminal voltage increases with decreasing temperature. This is somewhat surprising as one would typically expect the solar panel to operate more efficiently as temperature increases. However, one of the reasons the solar panel operates more efficiently with decreasing temperature is due to the electron and hole mobility of the semiconductor material. As temperature increases, the electron and hole mobility in the semiconductor material decreases significantly [6]. The electron mobility for Silicon at 25º C is about 1700cm^2/volt-sec and will decrease to about a fourth of this value as temperature increases to 225º C, and likewise the hole mobility decreases from about 600cm^2/volt-sec at 25º C to 200cm^2/volt-sec as temperature increases to 225º C. While the higher reference temperatures are not realistic operating conditions for a solar panel, it does show that electron and hole mobility decrease with increasing temperature.

The band gap energy of semiconductor materials also varies with temperature. An increase in temperature will cause the band gap energy of the material to increase. With higher band gap energy, the electrons in the valence band will require more energy from the photons to move to the conduction band. This means that a lot more photons will not have sufficient energy to be absorbed by the electrons in the valence band resulting in fewer electrons making it to the conduction band and a less efficient solar cell.

It should be noted here that irradiance and temperature represent only two of the most significant external factors that affect the efficiency of a solar cell; inclination, location, time of the year are also factors that affect the efficiency of solar cells. Additional parameters of a solar cell can be discussed by an illustration of the maximum power point as shown in Fig. 2.5.

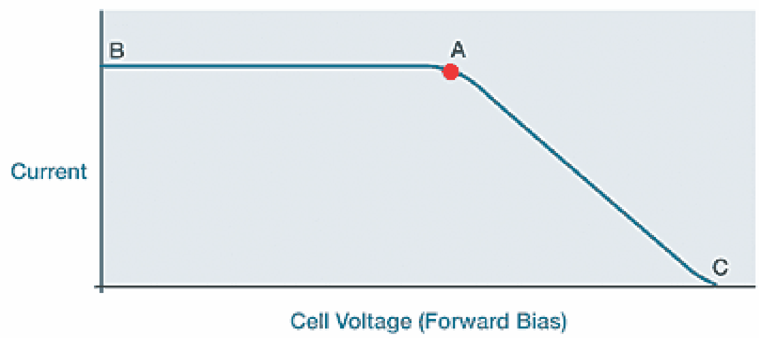

Fig. 2.5: Illustration of maximum power point

The cell's short circuit current intersects the Y-axis at point B and the open circuit voltage intersects the X-axis at point C. To achieve maximum energy transfer, systems powered by solar cells should be designed to transfer energy to the load at point A on the I-V curve. No energy should be delivered at points B and C, and most of the energy should be delivered as the operating point approaches point A. In a solar panel array, it is even more important that load impedance and source impedance are well matched. Once the cells are matched by their I-V characteristics, they can be grouped into individual arrays and each array is then made to operate at its maximum energy transfer point.

Majority of solar cells have high capacitance associated with their forward biased p-n junctions because the charged carriers are much closer together. The unwanted capacitance increases as the size of the solar cell and junction area increases. The I-V curve of the solar cell can be determined by taking fast I-V measurements which is done by applying a constant voltage and measuring the resulting current for the device being tested. However the high capacitance makes it difficult to get fast I-V measurements.

The shape of the I-V curve of the solar cell is governed by the cell's high Thevenin equivalent impedance [7]. The short circuit current is determined by the incident light intensity and it is inversely proportional to the applied voltage. The total circuit voltage and incident light determine the external circuit current.

2.3 Charge Application and MPPT Controllers

Solar panels are rarely connected directly to a load, but rather are used to charge energy storage components, such as batteries or ultra-capacitors. In most cases, the battery charging voltage determines the solar panel operating voltage. The battery charging voltage is usually not the most efficient operating voltage for the solar cell and therefore the most power is not being extracted from the solar cell. There also exists a possibility of overcharging when the solar panel is connected directly to a battery and overcharging can damage the battery. To avoid these potential problems, a charge controller is inserted between the solar panel and the battery or ultra-capacitor. The most commonly used type of charge controllers include basic charge controllers, Pulse Width Modulation (PWM) charge controllers and Maximum Power Point Tracker (MPPT) charge controllers.

The simplest form of charge controllers is the basic charge controller. These are usually designed to protect overcharging or undercharging of batteries which can cause damage to the battery. Continually supplying a charging current to a fully charged battery will increase the battery voltage causing it to overheat and damage. The basic charge controller simply monitors the state of charge of the battery to prevent overcharge. This form of charge controller regulates the voltage supply to the battery and cuts off supply once the battery reaches it maximum charge state. Overcharging some batteries can lead to explosions or leaking.

On the other hand, undercharging a battery for sustained periods will tend to reduce the life cycle of the battery. The charge controller monitors the state of charge of the battery to prevent it from falling below the minimum charge state. Once a battery reaches its minimum charge state, the charge controller disconnects the battery from any load to prevent the battery from losing any more charge. The basic charge controllers are usually operated by a simple switch mechanism to connect and disconnect the battery from the solar panel or load to prevent overcharging and undercharging.

While the basic charge controller is only able to connect or disconnect the battery from the solar panel to prevent overcharging, PWM charge controllers are able to regulate the charging current to the battery in order to optimize the charging time. As the battery approaches its maximum charge state, the PWM charge controller switches the charging on and off using pulse width modulation to slowly charge the battery. Slowly charging the battery as it approaches maximum capacity optimizes the speed and efficiency at which the battery is charged [8]. Both the basic charge controller and the PWM charge controller control the charging current going into the battery but do not address the operating efficiency of the solar panel.

The drawback of both the basic charge controller and the PWM charge controller is that they operate the solar panel at the battery charging voltage. For a vast majority of solar panel designs and applications, setting the solar panel voltage to the battery charging voltage causes the solar panel to operate away from its optimal operating point. Since the maximum operating point on the I-V curve of the solar panel varies with irradiance and temperature, operating the solar panel at a fixed point as the basic and PWM charge controllers do will guarantee that the solar panel will mostly operate away from its maximum power point.

Maximum Power Point Tracker charge controllers optimize the power output of the solar cell while also charging the battery to its optimal state. The MPPT constantly tracks the varying maximum operating point and adjusts the solar panel operating voltage in order to constantly extract the most available power. The MPPT charge controller maximizes solar cell efficiency while also controlling the charging state of the battery. The MPPT charge controller is basically a DC-DC converter that accepts a DC input voltage and outputs a DC voltage higher, lower or the same as the input voltage. This capability of the converter makes it ideal for converting the solar panel maximum power point voltage to the load operating voltage. Most MPPT charge controllers are based on either the buck converter (step-down), boost convert (step-up) or buck-boost converter setup [9].

2.4 Fuel Cells

Fuel cells are electrochemical devices that generate electrical energy by harnessing the energy produced during a chemical reaction. Fuel cells convert hydrogen and oxygen into water and in the process generate electricity. There are several different approaches to designing fuel cells, and they vary by chemistry. However, fuel cells are usually classified by the type of electrolyte that is used in the chemical process. The proton exchange membrane fuel cell (PEMFC) is one of the most promising technologies [10].

The fuel cell unit selected for the MRDEG system, the IdaTech FCS1200, is a proton exchange membrane type of fuel cell. The IdaTech FCS1200 uses a methanol and de-ionized water mix to generate high purity hydrogen, which is then stripped of electrons to create the hydrogen ion [11]. The hydrogen ion passes through the PEM and in the process electricity is generated. The hydrogen ion, stripped electrons and oxygen in air combine to form water. The fuel cell has a peak power of 2000W for sixty seconds at DC and it is able to continually output 1000W.

Additional specification about the IdaTech FCS1200 fuel cell including the manufacturer's Data Sheet is provided in the appendix.

2.4 Energy Storage Devices

Ultra-capacitors are used in parallel with battery banks to store the energy produced by the PV module. The ultra-capacitor is an electrochemical capacitor that is able to store a very large amount of energy relative to its size and weight. The ultra-capacitor is used as the main energy storage element since it provides much faster charge and discharge times and it also has a much longer life cycle than batteries. The high-energy battery bank is included in the system for reduced cost.

The ultra-capacitor and battery operating voltage is assumed to be 12V for our system, which is typical for many DC applications. The PV module initially charges the ultra-capacitor to the operating voltage and once the ultra-capacitor is fully charged, the battery bank begins to charge. A blocking diode is placed between the ultra-capacitor and the battery in order to prevent damage to the battery that might arise due to excessive currents between the two components. The blocking diode ensures that the current flows in only one direction: from the ultra-capacitor to the battery.

The Maxwell BOOSTCAP ultra-capacitor is selected for the project and additional specification about the ultra-capacitor is provided in the appendix.

CHAPTER 3

Analysis and Modeling of MRDEG System and MPPT Circuit

3.1 System Architecture and Description

Solar and fuel cells will be the main energy source for a future Multi-Source Renewable Distributed Energy Generation (MRDEG) System. Multiple solar photovoltaic cell (PVC) arrays will be operated as subsystems in parallel connection with fuel cell arrays and high-density energy storage components, including super-capacitors. All the components of the proposed MRDEG system are arranged in such a way as to achieve maximum power output at a minimum cost under various operating condition.

This new system also consists of a multi-function power converter supporting multi-source renewable distributed energy units (MSREU). The PV modules act as the primary source of energy and consist of single solar panels arranged in series and parallel to match the voltage and power output requirement. The fuel cell modules act as backup in periods of no sunlight and when the energy storage devices are discharged. A block diagram of the optimal architecture for the system is shown in Fig. 3.1 below.

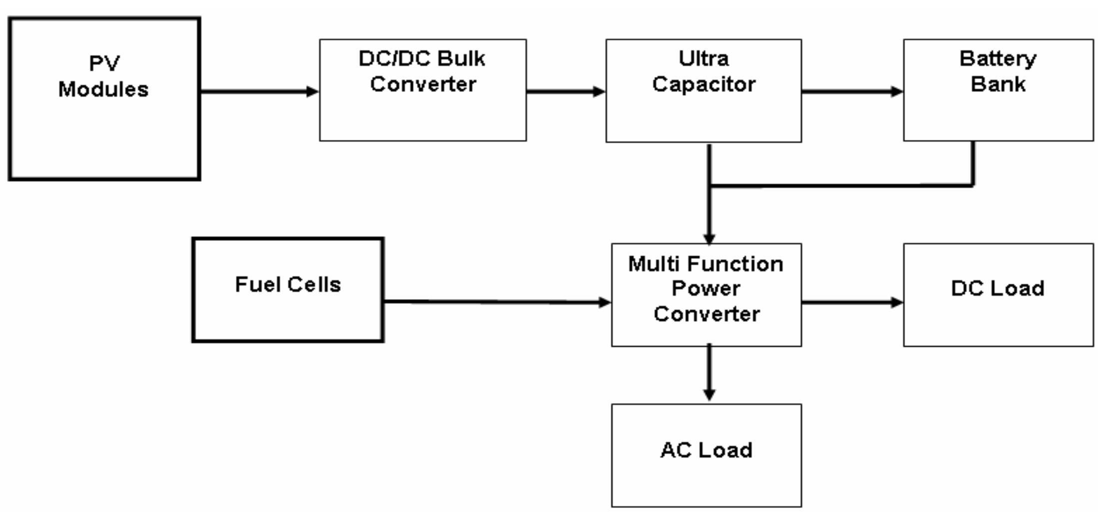

Fig 3.1: Block diagram showing optimal layout of MRDEG system

One of the core technologies of the MRDEG system is the advanced multi-function power converter that also provides an integrated system control to manage the power flow between supply components and AC or DC load.

Ultra-capacitors are used in parallel with batteries to store the energy produced by the PV modules. Ultra-capacitors are used because they provide much faster charge and discharge times and also a much longer life cycle than batteries [12]. The PV modules directly feed the DC-DC buck converter. A blocking diode is placed between the ultra-capacitor and the battery to prevent excessive currents between the two components. The buck converter is operated by a feedback PWM controller that monitors the incoming voltage and current levels and controls the buck converter accordingly [13]. The ultra-capacitors and batteries then feed AC and DC loads through the power converter during sunlight hours and at nighttime.

3.2 Modeling of Key Components and Subsystems

To properly model a solar cell and subsystems, it is important to understand how solar cells operate and how a simple PSpice model can be generated. Solar cells are primarily made of semiconductor material that when exposed to light induce a process of photon reflection and absorption, generation of free carriers and lastly charge separation, which creates an electric field. The semiconductor properties determine how effectively this process occurs. Some of the most important properties include the absorption coefficient, the reflectance of the semiconductor surface, drift-diffusion parameters and surface recombination velocities.

The absorption coefficient depends on the value of the bandgap of the semiconductor material and the nature of the bandgap. Absorption coefficient values for the most commonly used semiconductor materials are widely available. The reflectance of the semiconductor surface depends on the surface finishing, particularly the shape and antireflection coating. Drift-diffusion parameters control the migration of charge towards the collecting junction; the parameters are carrier lifetimes, and mobilities for electron and holes. It is also important to know the surface recombination velocities at the surface of the solar cell where minority carriers recombine. These factors effectively determine how much of the sun's energy a solar cell can capture and successfully convert to electrical energy.

For practical power applications, the voltage produced by one solar cell is usually not sufficient to power most equipment. An array of between 20 to 80 solar cells connected in series to form a "Solar Module" is usually necessary to provide the required voltage. Solar cell manufacturers can provide some key parameters of a solar module in their Data Sheet. The output power is given in W_p (Watt peak), which means the module was rated at Standard Test Conditions (STC). The STC are an illumination level of 1000 W/m^2 (bright sunshine), a spectrum equivalent to AM 1.5 and 25°C module temperature at the test. The manufacturer's data sheet also provides the short circuit current, the current produced when the output voltage is zero, and the open circuit voltage, the voltage across the output terminals when there is no current flowing in the cell.

A simplified equivalent circuit of a solar cell consists of a diode and a current source which are switched in parallel. The photocurrent generated when the sunlight hits the solar panels can be represented with a current source and the p-n transition area of the solar cell can be represented with a diode.

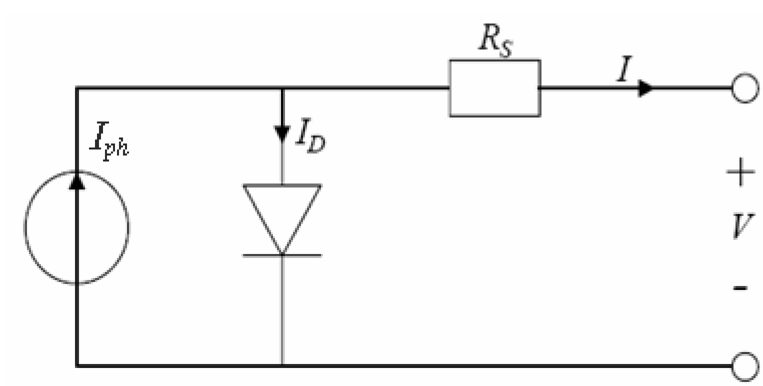

Fig 3.2: Simplified equivalent circuit of solar cell

The voltage and current relationship of the simplified solar cell can be derived from Kirchoff's current law. According to Kirchoff's current law, all currents entering and leaving a node add up to zero.

Thus,

$$I = I_{Ph} - I_D = I_{Ph} - I_S \cdot \left[\exp\left(\frac{V}{m \cdot V_T}\right) - 1 \right] \tag{3.1}$$

where

I_{Ph} is the photocurrent

I_D is Diode current

I_S is Diode reverse saturation current

m is Diode ideal factor

V_T is Thermal voltage (25.7mV at 25°C)

This simplified equivalent circuit, however, does not give an accurate representation of the electrical process at the solar cell. On real solar cells, voltage losses occur at the boundary and external contacts and leakage currents occur throughout the cell; these losses can be represented with a series resistance R_S and a parallel resistance R_P respectively. The equivalent circuit of the solar cell showing the series and parallel resistance is shown below

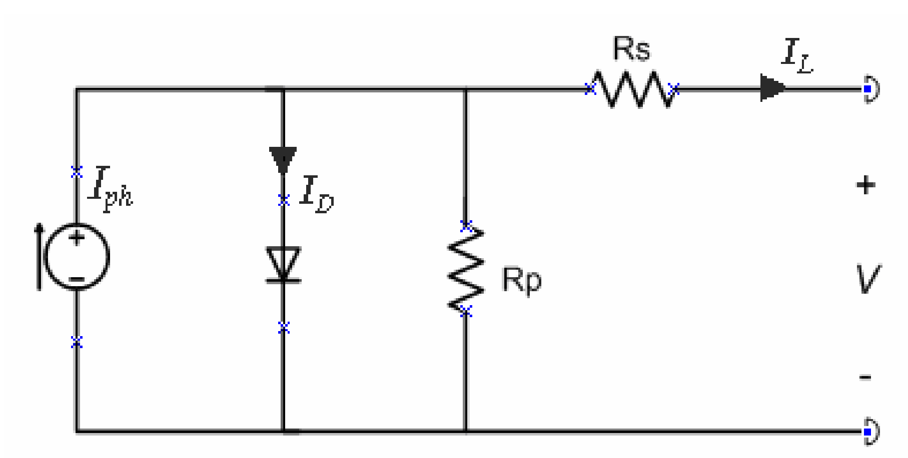

Fig 3.3: Equivalent circuit of solar cell showing ext resistances

The voltage and current relationship can also be derived from Kirchoff's current law:

$$I_P = \frac{V_D}{R_P} = \frac{V + I \cdot R_S}{R_P} \tag{3.2}$$

$$I_{Ph} - I_S \cdot (\exp(\frac{V + I \cdot R_S}{m \cdot V_T}) - 1) - \frac{V + I \cdot R_S}{R_P} - I = 0 \tag{3.3}$$

As an example, a practical solar module selected for our lab experimental system is the Sharp NE-80EJEA solar cell. The solar module is able to output a maximum power of 80W. The specifications of the solar module and I-V characteristic curves as well as the maximum power operating curves are supplied by the manufacturer's data sheet as shown in Fig. 3.4 and Fig. 3.5.

ELECTRICAL CHARACTERISTICS	
Cell	Poly-crystalline silicon
No. of Cells and Connections	36 in series
Open Circuit Voltage (Voc)	21.6V
Maximum Power Voltage (Vpm)	17.3V
Short Circuit Current (Isc)	5.16A
Maximum Power Current (Ipm)	4.63A
Maximum Power (Pmax)*	80W (+10% / -5%)
Module Efficiency (ηm)	12.40%
Maximum System Voltage	600VDC
Series Fuse Rating	10A
Type of Output Terminal	Junction Box

Fig 3.4: Electrical characteristics of Sharp NE-80EJEA solar cell

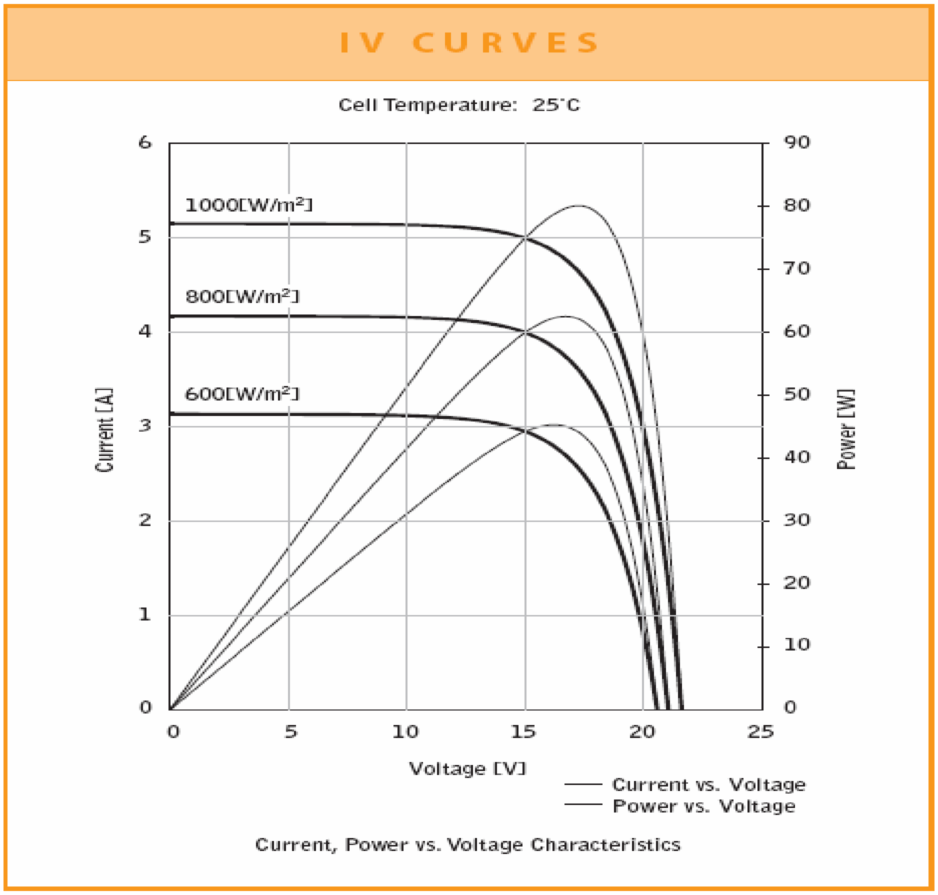

Fig 3.5: I-V characteristic curve of Sharp NE-80EJEA solar cell

3.2.1 Solar Cell Math Model

A math model of the selected PV module will be given in this section. It can be used in the determination of the voltage and current at which the maximum power is extracted from the solar cell.

The current through the solar cell can be derived from

$$I = I_S(e^{\frac{V}{V_T}} - 1) - I_{ph} \tag{3.4}$$

Note that this expression is a simplified form of the equation provided earlier as it does not include the diode ideal factor, essentially ignoring the recombination in the depletion region. The photocurrent, I_{ph}, is assumed to be independent of applied voltage and I_S is the saturation current of the diode.

The short circuit current, I_{sc}, is the current with no voltage applied and equals

$$I_{sc} = -I_{ph} \tag{3.5}$$

The open circuit voltage, V_{oc}, is the voltage with zero current and equals

$$V_{oc} = V_T \ln\left(\frac{I_{ph}}{I_S} + 1\right) \approx V_T \ln\frac{I_{ph}}{I_S} \tag{3.6}$$

The total power dissipated equals

$$P = V \times I = I_S V\left(e^{\frac{V}{V_T}} - 1\right) - I_{ph} V \tag{3.7}$$

By taking into account that maximum power occurs when $\frac{dP}{dV} = 0$, it is possible to derive the maximum voltage point, V_m, and the maximum current point, I_m, as

$$\frac{dP}{dV} = 0 = I_S\left(e^{\frac{V_m}{V_T}} - 1\right) - I_{ph} + \frac{I_S V_m}{V_T} e^{\frac{V_m}{V_T}} \tag{3.8}$$

At the maximum power point equation can be rewritten as

$$V_m = V_{oc} - V_T \ln\left[1 + \frac{V_m}{V_T}\right] \tag{3.9}$$

V_m can be calculated by solving the transcendent equation above provided V_{oc} is known.

$$I_m = I - I_0\left(e^{\frac{V_m}{V_T}} - 1\right) \tag{3.10}$$

The maximum power, P_m, can be approximated by`

$$P_m = I_m \times V_m \approx -I_{ph}\left(1 - \frac{V_T}{V_m}\right)\left(V_{oc} - V_T \ln\left(1 + \frac{V_m}{V_T}\right)\right) \tag{3.11}$$

$$P_m \approx -I_{ph}\left(V_{oc} - V_T \ln\left(1 + \frac{V_m}{V_T}\right) - \frac{V_{oc} V_T}{V_m}\right) \tag{3.12}$$

For the Sharp NE-80EJEA solar cell, the following parameters are determined by the manufacturer as:

$$\boxed{V_m = 17.3\text{ V}}$$

$$\boxed{I_m = 4.63\text{ A}}$$

$$\boxed{P_m \approx V_m \times I_m = 80.01\text{ W}}$$

Another interesting parameter of a solar cell math model is the *fill factor (FF)*. The fill factor is defined as the ratio between the maximum power P_m and the $I_{sc} V_{oc}$ product; the conversion efficiency is defined as the ratio between the solar cell output power and the solar power impinging the solar cell surface

$$FF = \frac{V_m I_m}{V_{oc} I_{sc}} \tag{3.13}$$

$$\eta = \frac{V_m I_m}{P_{in}} = FF \frac{V_{oc} I_{Sc}}{P_{in}} \tag{3.14}$$

For our lab prototype solar cell the fill factor is 0.718.

3.2.2 Solar Cell Circuit Model

A model of the Sharp NE-80EJEA solar cell is implemented in Pspice. From the electrical characteristics of the solar cell, it is apparent that the solar cell is a non-linear device. One approach to handling non-linear circuits in Pspice is to define subcircuits for the main blocks. Using subcircuits to model the solar cell is particularly helpful when connecting several solar cells in series or in parallel as required for the application.

The Pspice model of the subcircuit of an ideal solar cell is the circuit representation of the current equation (3.4) of a solar cell. The short circuit current is proportional to the irradiance that the solar cell receives, and in order to implement this relationship in Pspice, the value of the short circuit current is assigned to a voltage-controlled current source (known as a G-device in Pspice). The G-device used is named 'gsource' and is given by

$$gsource = \frac{J_{sc}A}{1000}G \tag{3.15}$$

Where A is the solar cell surface area, J_{sc} is the short-circuit current density under standard (AM1.5G, 1000 W/m^2, 25 ºC cell temperature), and G is the value of the irradiance in W/m^2. The above equation gives the value of the short circuit current at any irradiance value G, so long as the proportionality between irradiance and short circuit current holds.

The solar cell subcircuit is connected to an external measurement circuit in order to obtain the I-V characteristic. The external circuit includes a DC bias voltage source which is swept from 0v to 600mV. A PSpice model of the solar cell is shown below in Fig. 3.6. The single solar cell is successfully modeled and simulated and the I-V characteristic is shown in Fig. 3.7.

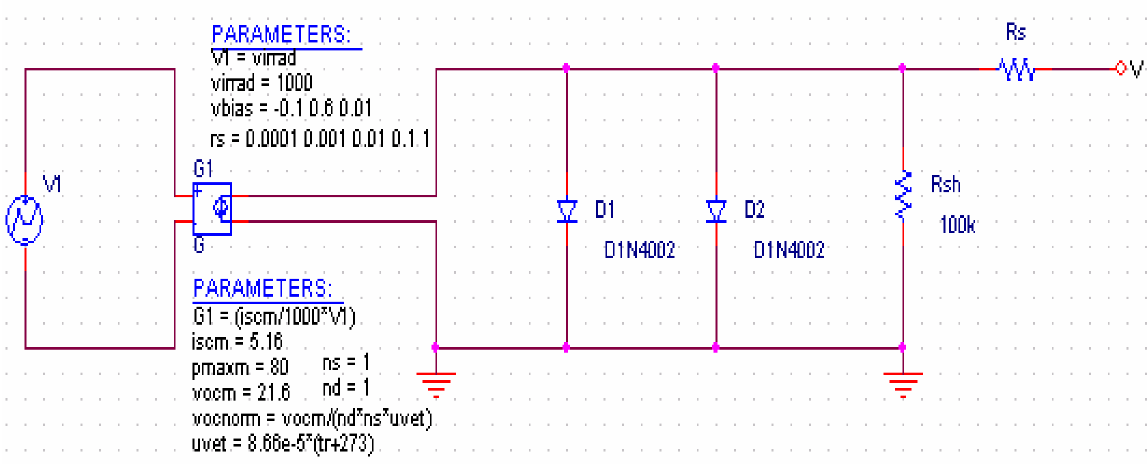

Fig 3.6: PSpice circuit model of solar cell

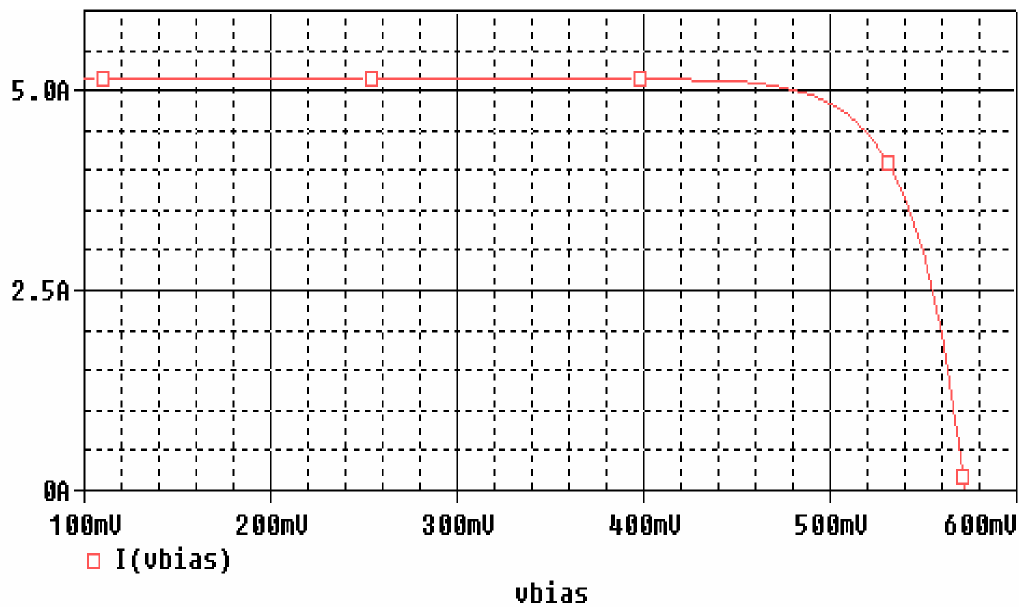

Fig 3.7: I-V characteristic for a single solar cell

The intersection of the graph with the y-axis gives the value of the short circuit current of the solar cell, which in this case corresponds to 5.16A. The open circuit voltage for each cell can also be derived from the I-V plot. The crossing of the I-V curve with the voltage axis is the open circuit voltage, which corresponds to almost 600mV for each individual solar cell. According to the specifications supplied in the Manufacturer Data Sheet (MDS) of the Sharp NE-80EJEA, there are 36 cells connected in series, hence the total open circuit voltage is 600mV × 36 = 21.6V.

From the equation of the open circuit voltage (3.6), it is observed that the value of the open circuit voltage depends logarithmically on the I_{ph} / I_S ratio. This implies that under constant temperature the value of the open circuit voltage scales logarithmically with the short circuit current, but since the short circuit current scales linearly with irradiance, it means the open circuit voltage is logarithmically dependent on the irradiance. This important relationship indicates that the effect of irradiance is much larger in the short circuit current that in the open circuit voltage value.

The selected solar module represents 36 identical solar cells connected in series, with the same irradiance value. The I-V characteristic of the solar module is expected to have the same short circuit current as a single solar cell while the voltage drop is 36 times the voltage drop in one solar cell. The I-V characteristic of the solar module is shown below in Figure 3.8.

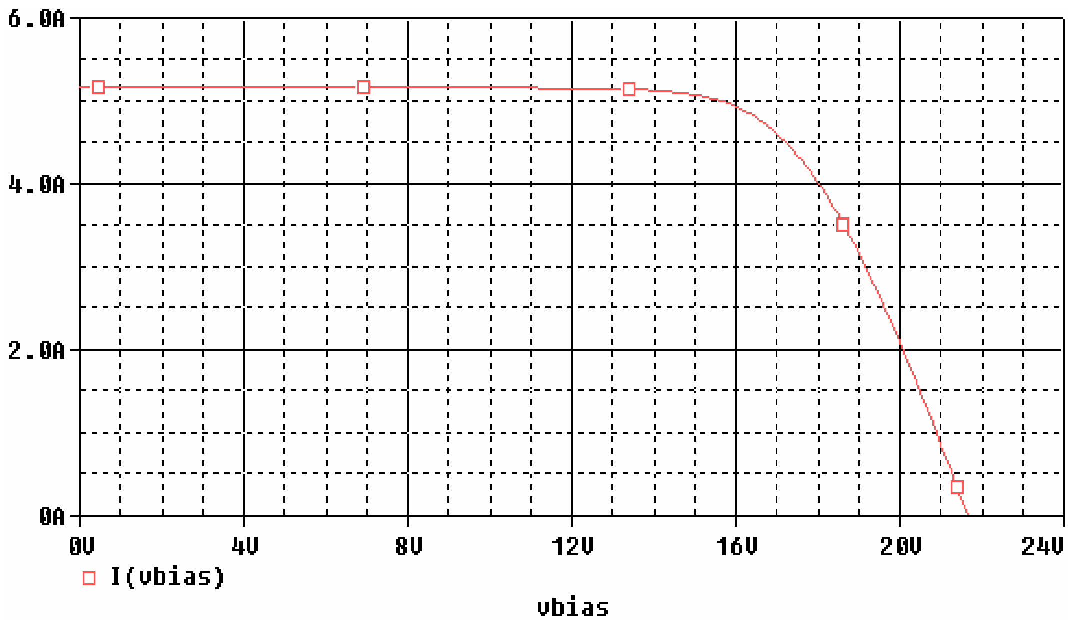

Fig 3.8: I-V characteristic of solar module consisting 36 individual solar cells

The output power of the solar cell is the product of the output current delivered to the load and the voltage across the cell. The power at any point of the I-V characteristic is given by equation (3.7). There is no power output at the short circuit point where the voltage is zero and also at the open circuit point where the current is zero. Power is generated between the short circuit point and the open circuit point on the I-V characteristic. Somewhere on the characteristic, between the two zero points, there exist a point where the solar cell generates the most power. The point is called the maximum power point (MPP). A plot of the I-V characteristic including the output power of our solar cell is shown in Fig. 3.9.

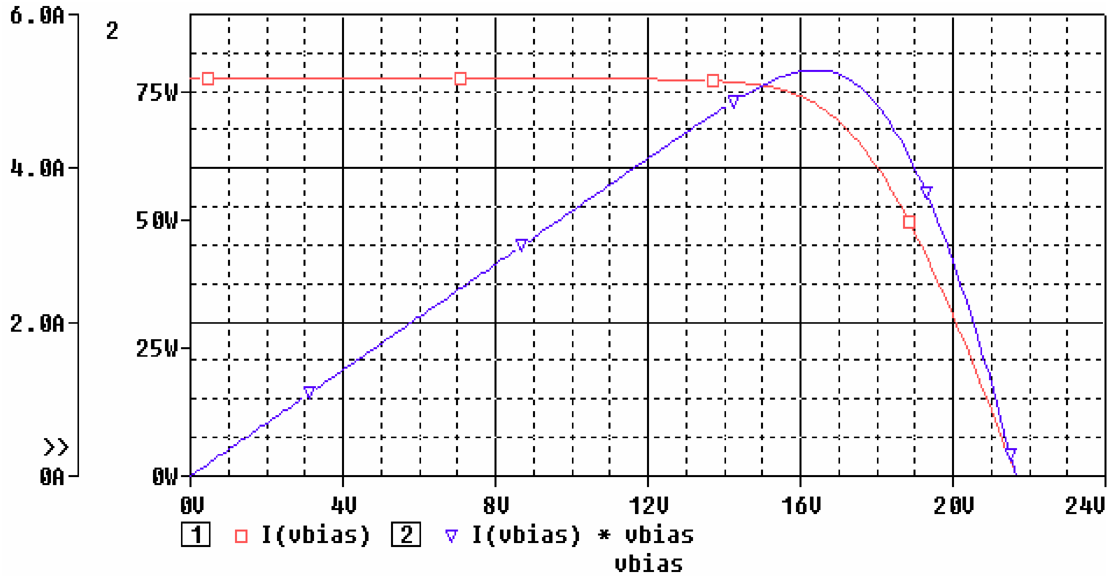

Fig 3.9: I-V characteristic and output power for the Sharp NE-80EJEA solar cell

3.3 MPPT Requirements and Circuit Description

The Maximum Power Point Tracker (MPPT), a type of charge controller, is an electronic system that operates the PV module in a way that allows the module to produce the maximum power. Without an MPPT charge controller, the operation of a solar module with a conventional (non-MPPT) charge controller is as follows: for a conventional controller charging a load, e.g. battery, the solar modules are connected directly to the load. This forces the modules to operate at the load voltage, say 12V for the battery, but this is typically not the optimal operating voltage at which the modules are able to produce their maximum power.

For example, the PV module I-V/power characteristic for our prototype solar cell in Fig 3.8 shows that for a solar module connected directly to a battery load, the operating voltage of the solar module is clamped to the battery charging voltage of $V_b \leq 12V$. By forcing the solar module to operate at $V_b \leq 12V$, the power produced is artificially limited to less than approximately 60W, but the solar module is actually capable of delivering a maximum of 80W. Hence the solar module is operating 33% less efficiently than if it were able to produce its maximum power.

Introducing an MPPT charge controller will allow more power to be produced by the solar module [13]. First, the operating voltage at which the solar module produces the most power must be determined. Then a high efficiency DC-DC power converter is used to adjust the solar module maximum power voltage at the converter input to the battery charging voltage at the converter output. From the I-V/Power characteristic of our solar module, the maximum power point is estimated at 17V. The MPPT system is made to operate the solar module at 17V, thus extracting the full 80W, regardless of the load voltage. Assuming an ideal system, the battery charging current would now be a ratio of the module operating voltage and the battery charging voltage multiplied by module operating current ($17\text{V} \div 12\text{V} \times 4.7\text{A} = 6.66\text{A}$). This represents a charge current increase of about 1.5A or 29% that would have been wasted using a conventional charge controller. This gain will be somewhat smaller under normal operating conditions due to non-ideal power losses associated with the system.

Apart from improving charging efficiency for battery loads and other energy storage elements, MPPT charge controllers are particularly useful in applications where the life of the load can be strongly reduced when forced to work in extreme conditions [14]. A solar module's operating condition may vary as the weather outside becomes hot or due to partial shading of the solar panels. The MPPT ensures that applications such as DC motor water pumps are not forced to work outside their safe operating area (SOA).

The main component of the MPPT in this example system is the DC-DC buck converter that steps down the solar panel output voltage to the desired load voltage. To ensure that the solar module operates at the maximum operating point, the input impedance of the DC-DC converter must be adapted to force the solar module to work at its maximum power point [15]. Depending on the load requirement, other types of DC-DC converters can be employed in the MPPT design. For example, the boost converter is able to output a higher voltage from a nominal input voltage; other types of DC-DC converter include the buck-boost converter, CuK converter and full-bridge converter [16].

The buck converter uses energy storage components such as inductors and capacitors to control the energy flow from the solar module to the load by continuously opening and closing a switch. The switch is usually an electronic device that operates in two states: in the conduction mode (on), the output of the solar cell in connected to an inductor while in the cut-off mode (off), the output of the solar module is disconnected from the inductor. The buck converter also contains a forward biased diode that provides a return path for the current in the cut-off state. The basic circuit for the buck converter is shown below in Figure 3.10.

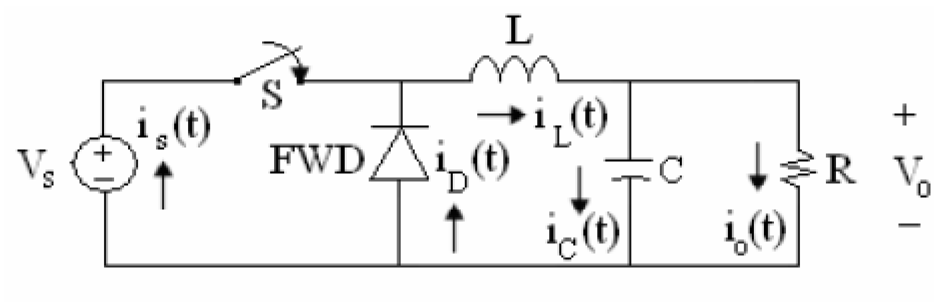

Fig 3.10: Basic circuit of a buck converter

The switch is actually a MOSFET that is controlled by a PWM signal. The switch conducts on and off to control the voltage level at the inductor. The voltage at the inductor has a rectangular waveform that is later filtered by the LC combination to produce a quasi-continuous voltage at the output. The average value of the rectangular waveform can be adjusted to control the length of the conduction and cut-off states of the switch. The on time of the switch is related to its time period such that $t_{on} = DT$, where D is the duty cycle. In the ON state, current flows from the module through the inductor causing the inductor to store energy. In this state the diode is in reverse bias and no current flows through it. In the OFF state, the off time is given by $t_{off} = (1 - D)T$ and the current in the inductor causes the diode to become forward biased. The diode turns ON and provides a path to maintain the continuity of current through the inductor.

The duty cycle can be adjusted to set the output voltage of the converter to the desired value. For an ideal DC-DC converter, the duty cycle is the ratio between the output voltage and the input voltage, $D = V_o / V_i = I_i / I_o$. For our system, the DC-DC converter is used as a DC power supply, where the input voltage varies with temperature and insolation conditions, but the output voltage is maintained at a desired value. This allows the duty cycle to be set such that the input voltage to the DC-DC converter is always set at the solar module's maximum power point voltage. The duty cycle is set by means of a pulse width modulation (PWM) signal used to control the MOSFET on and off states.

3.3.1 MPPT System Analysis

The buck converter contains two energy storage elements, the inductor and capacitor. The two elements result in a second order differential equation for both the inductor current and the capacitor voltage. The differential equation for the capacitor voltage, in the ON state, is given by

$$LC\frac{d^2V_C(t)}{dt^2} + \frac{L}{R}\frac{dV_C(t)}{dt} + V_C(t) = V_i \tag{3.16}$$

Assuming that the voltage across the load, and thus the capacitor, is constant, then the differential equation above can be simplified and can be written for the current through the inductor as

$$L\frac{di_L(t)}{dt} = V_i - V_o \tag{3.17}$$

If the circuit has been on for some time and is now in steady state, the solution for the current through the inductor yields

$$i_L(t) = \frac{V_i - V_o}{L}t + I_{L,0} \tag{3.18}$$

Where $I_{L,0}$ is the current in the inductor just before the switch is turned on. The inductor current increases linearly with time and attains it final value, I_L, as $t \to t_{on} = DT$

$$I_L = \frac{V_i - V_o}{L}DT + I_{L,0} \tag{3.19}$$

The difference between the final and initial value of the inductor current is called the peak-to-peak current ripple ΔI_L, and is given by

$$\Delta I_L = I_L - I_{L,0} = \frac{V_i - V_o}{L} DT \tag{3.20}$$

The current ripple is directly proportional to the duty cycle, D, and inversely proportional to the inductance, L. Thus, the current ripple can be controlled by the duty cycle or with proper selection of the inductor.

For the OFF state, the inductor current flows through the diode and the first order differential equation is given by

$$L\frac{di_L(t)}{dt} = -V_0 \tag{3.21}$$

The solution of the differential equation yields

$$i_L(t) = \frac{-V_0}{L}t + I_L \tag{3.22}$$

Here I_L is the value of the current in the inductor just as the switch is opened. The inductor current decreases to its minimum value, $I_{L,0}$, as $t \to t_{off} = (1-D)T$

$$I_{L,0} = -\frac{V_0}{L}(1-D)T + I_L \tag{3.23}$$

The equation gives a peak-to-peak current ripple equation

$$\Delta I_L = I_L - I_{L,0} = \frac{V_0}{L}(1-D)T \tag{3.24}$$

The above equation can be simplified to

$$V_o = DV_i \tag{3.25}$$

The waveform of the inductor current is shown below

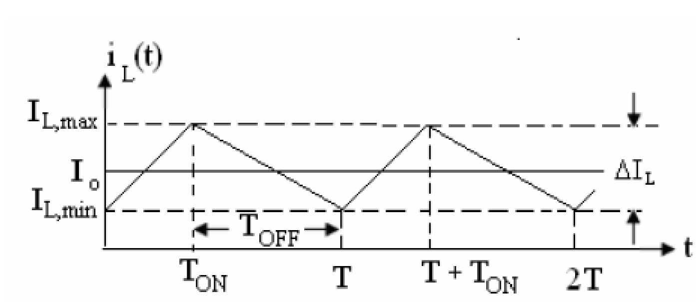

Fig 3.11: Waveform of inductor current

The average current in the inductor is equal to the DC current through the inductor

$$I_{L,avg} = I_o = \frac{V_o}{R} \tag{3.26}$$

Using the equation above, the maximum current through the inductor is

$$I_L = I_{L,avg} + \frac{\Delta I_L}{2} = \frac{V_o}{R} + \frac{V_o}{2L}(1-D)T \tag{3.27}$$

And the minimum current through the inductor is

$$I_0 = I_{L,avg} - \frac{\Delta I_L}{2} = \frac{V_o}{R} - \frac{V_o}{2L}(1-D)T \tag{3.28}$$

Assuming all the components are ideal and there is no power loss, the average power supplied by the source is equal to the average power delivered to the load [17], that is

$$V_i I_i = V_o I_o = D V_i I_o \tag{3.29}$$

Using the above equation, the average load current may be expressed in terms of the source current as

$$I_i = D I_o \tag{3.30}$$

The difference between the inductor current and the load current is the time-varying current through the capacitor. The maximum and minimum current through the capacitor are

$$I_C = \frac{\Delta I_L}{2} = \frac{V_o}{2L}(1-D)T \tag{3.31}$$

$$I_{C,0} = -\frac{\Delta I_L}{2} = -\frac{V_o}{2L}(1-D)T \tag{3.32}$$

The waveform for the current through the capacitor is shown below

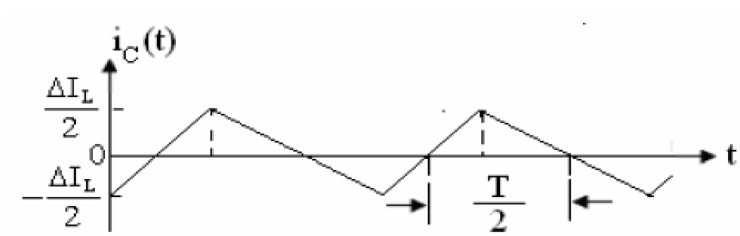

Fig 3.12: Waveform of the current through the capacitor

The average current through the capacitor is zero. During one-half cycle, the current is charging the capacitor and the increase in charge is given by

$$\Delta Q = \frac{1}{2}\frac{\Delta I_L}{2}\frac{T}{2} = \frac{1}{8}\Delta I_L T \tag{3.33}$$

The increase in capacitor voltage is

$$\Delta V_o = \frac{\Delta Q}{C} = \frac{1-D}{8LC}V_o T^2 = \frac{1-D}{8LCf^2}V_o \tag{3.34}$$

The capacitor ripple is the ratio of the increase in capacitor voltage to its average value and is given by

$$\frac{\Delta V_o}{V_o} = \frac{1-D}{8LCf^2} \tag{3.35}$$

To ensure that the buck converter operates in continuous conduction mode (CCM), i.e. the minimum current can be zero at the time of switching, a minimum value of the inductor is determined by

$$\frac{V_o}{R} - \frac{V_o}{2L_{\min}}(1-D)T = 0 \tag{3.36}$$

$$L_{\min} = \frac{1-D}{2}RT = \frac{1-D}{2f}R \tag{3.37}$$

3.3.2 Design of a MPPT System

A high frequency DC-DC buck converter consisting of two simple conversion stages is proposed for the maximum power point tracker. Each stage of the converter will be designed according to the MPPT system equations. The first stage of the converter, which maintains the output voltage of the solar module at the maximum power point, has a target output of approximately 17.3V. Since the actual power delivered by the solar module will vary with temperature and insolation conditions, it is necessary to initially assume a fixed operating voltage in determining the parameters of the devices to be used.

For our case, an open-circuit voltage of 20V has been selected. This operating voltage is used to select an initial duty cycle for the MOSFET and also choose appropriate element values. Once the device parameters have be chosen, the feedback mechanism of the MPPT will dynamically adjust the duty cycle according to the actual operating condition of the solar module. Thus, the fist stage of the buck converter has the following properties:

The duty cycle, from equation (3.24), is

$$D = \frac{17.3}{20} = 0.865$$

The time period is

$$T = \frac{1}{f} = \frac{1}{33000} = 30.3\mu s$$

The on and off times for the switch are

$$t_{on} = DT = 0.865 \times 30.3 \times 10^{-6} = 26.2\mu s$$

$$t_{off} = (1 - D)T = (1 - 0.865)(30.3 \times 10^{-6}) = 4.09\mu s$$

The equivalent resistance is

$$R = \frac{V_o^2}{P} = \frac{17.3^2}{80} = 3.74\Omega$$

The minimum value of the inductor for CCM, from equation (3.37), is

$$L_{\min} = \frac{1 - D}{2f} R = \left(\frac{1 - 0.865}{2 \times 33{,}000} \right) (3.74) = 7.65\mu H$$

Assuming a voltage ripple of 1%, the value of the capacitor is

$$C = \frac{1 - D}{8L \frac{\Delta V_o}{V_o} f^2} = \frac{1 - 0.865}{8 \times 7.65 \times 10^{-6} \times 0.01 \times 33{,}000^2} = 202\mu F$$

Similarly for the second stage of the buck converter, which maintains the output voltage at 12V regardless of load variations, the properties are as follows:

The duty cycle is

$$D = \frac{12}{17.3} = 0.694$$

The time period is

$$T = \frac{1}{f} = \frac{1}{33000} = 30.3\mu s$$

The on and off times for the switch are

$$t_{on} = DT = 0.694 \times 30.3 \times 10^{-6} = 21\mu s$$
$$t_{off} = (1-D)T = (1-0.694)(30.3 \times 10^{-6}) = 9.27\mu s$$

The equivalent resistance is

$$R = \frac{V_o^2}{P} = \frac{12^2}{80} = 1.8\Omega$$

The minimum value of the inductor for CCM, from equation (3.37), is

$$L_{\min} = \frac{1-D}{2f}R = \left(\frac{1-0.694}{2 \times 33{,}000}\right)(1.8) = 8.35\mu H$$

Assuming a voltage ripple of 1%, the value of the capacitor is

$$C = \frac{1-D}{8L\dfrac{\Delta V_o}{V_o}f^2} = \frac{1-0.694}{8 \times 8.35 \times 10^{-6} \times 0.01 \times 33{,}000^2} = 420\mu F$$

3.3.3 MPPT Circuit Model in PSpice

The MPPT circuit model consists of two power conversion stages; the first stage matches the input of the converter to the maximum power point voltage of the solar module while the second stage matches the output load voltage. Therefore, two different control references are required to control the length of the conduction and cut-off times for each stage. As with the solar cell circuit model, the MPPT circuit is implemented in Pspice. Each stage of the power converter will consist of (i) an error amplifier to measure the difference between the output voltage and the desired reference voltage, and (ii) a PWM generator to control the MOSFET switch of the converter.

The error amplifier is an essential part of the feedback loop since it is able to adjust the input voltage to drive the buck converter to the desired output. The error amplifier measures how close the output voltage is to the desired voltage. The measurement of error is the difference between the output voltage and the reference voltage, $V_{ErrAmp} = k(V_o - V_{ref})$. In PSpice, the error amplifier is modeled with an operational amplifier that generates a voltage equal to the difference between the output voltage and the reference voltage. The error then drives the PWM circuit. The PSpice circuit diagram of the error amplifier is shown below

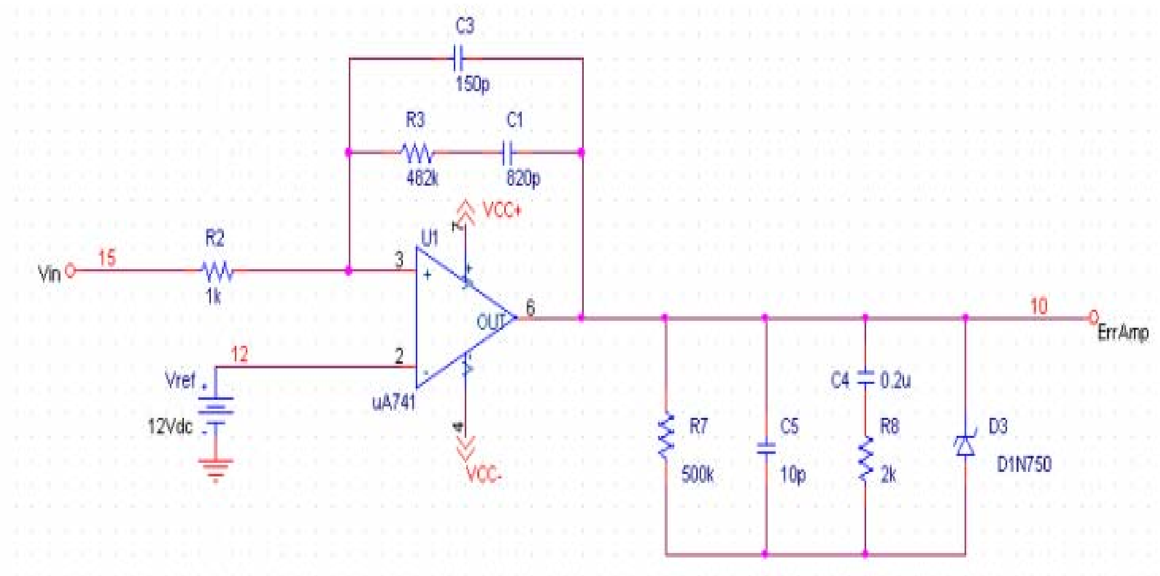

Fig 3.13: PSpice circuit schematic of error amplifier

A capacitor is added to model the bandwidth limit of the error amplifier. A low pass RC filter combination is also included to limit the high frequency gain of the amplifier; this is necessary to prevent wild ringing or oscillations [18]. Finally, a diode is added to clamp the error voltage to an appropriate range. The logic behind the error amplifier is as follows: (i) when the difference between the output voltage and the reference voltage is positive, the duty cycle is increased; (ii) when the difference is negative, the duty cycle is decrease; while the duty cycle is maintained when the difference between the output and reference voltage is zero.

A pulse width modulation signal is used to drive the MOSFET, which controls the power flow from the input to the output of the converter. Two main components are used to model the PWM: a triangle wave and a comparator. Pspice does not have a triangle wave generator/source, but a triangle wave can be achieved with a square wave generator with long rise and fall times. The comparator is achieved by the use of an operational amplifier and the TABLE function in Pspice. As the output of the error amplifier varies between zero and its maximum value, the PWM output changes from 0% to 100% duty cycle. The output of the PWM then drives the MOSFET switch. Since there are two stages in the MPPT design, each stage will require a unique PWM signal. The PSpice circuit diagram of the PWM is shown in Fig. 3.14 below

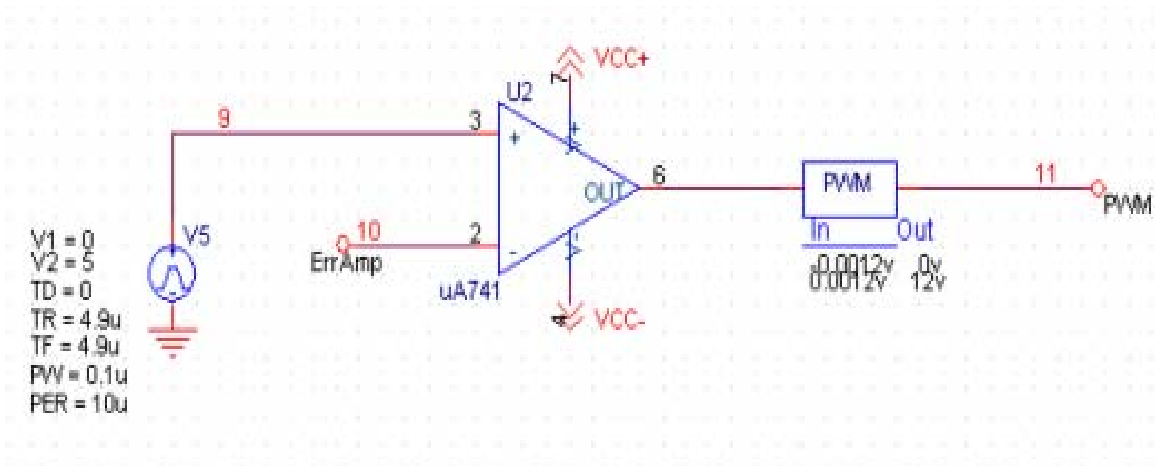

Fig 3.14: PSpice circuit schematic of PWM

The MPPT control circuit has implemented and evaluated by digital simulation in Pspice. The output of the error amplifier and the PWM are shown in Fig. 3.15. The complete schematic of the MPPT showing both stages of the power conversion is shown in Fig 3.16. For a convenient collation of the results, the maximum power point of the solar cell is assumed to be 80% of the open circuit voltage [19], V_{oc}, in our case $21.6\,\text{V} \times 0.8 = 17.28\,\text{V}$. Thus, the solar module is represented with discrete DC voltage sources ranging from 16V, under unfavorable weather conditions, to 21.6V, the open circuit voltage.

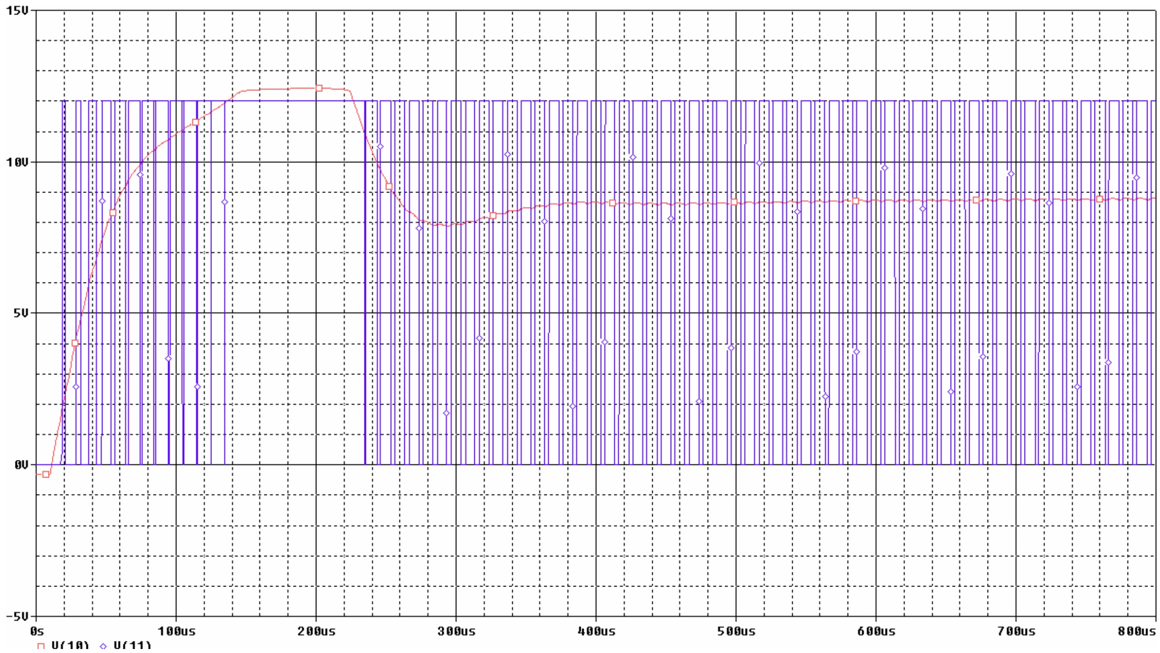

Fig 3.15: Control signal from error amplifier voltage and the PWM output

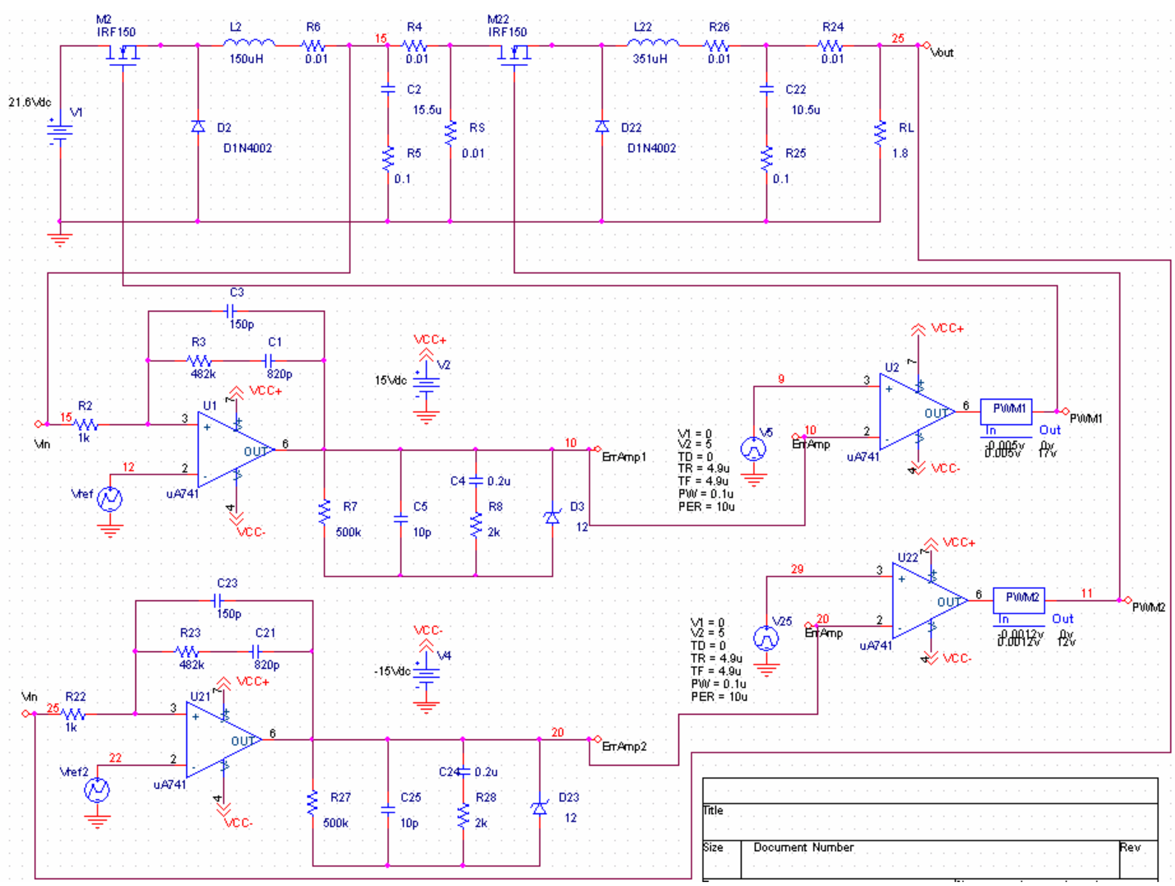

Fig 3.16: Schematic of two-stage MPPT in PSpice

CHAPTER 4

Discussion of Practical Circuit Elements

4.1 Component Selection

There are several factors to be considered when selecting the key devices or components to be used in the circuit of the maximum point power tracker, but one of the most important is the power loss associated with each device. Since the objective of the tracker is to deliver maximum power from the solar module to the load, power losses associated with the tracker itself should be minimal. The primary parts of the MPPT are simple and readily available components and they include the MOSFET, diodes, operational amplifiers, inductors, capacitors and resistors. Each component has some power loss associated with it. A power loss comparison is used to select the specific type of element that is best suited for the design.

There are three main types of power losses associated with the MOSFET: the first is due to the small internal resistance when in the conduction state, the second is due to the small internal capacitance at the gate of the MOSFET, and the third is due to the rise and fall times of the switch [20]. The on-resistance (r_{DS}) and gate-to-source charge (Q_{GS}) constitute a majority of the loss; the lower the r_{DS} and Q_{GS} values, the lower the power loss. The conduction loss due to the on-resistance of a MOSFET is a function the current passing through it: $P_{on} = I^2 R$.

The gate-to-source charge is the amount of charge required to close the MOSFET switch. A capacitor connected between the gate and the source of the MOSFET stores the charge and once enough charge has accumulated, the switch is closed allowing current to flow from the drain to the source. The charge stored in the capacitor dissipates once the switch is closed and this results in some power loss; the relationship between the amount of charge stored and the power loss is $P_{S1} = Q_{GS} V_{GS} f$. This power loss is dependent on the switching frequency.

The third form of power loss associated with the MOSFET is due to the rise and fall times of the device. When the MOSFET switches on, the switch is not instantaneous and there is some delay as the current begins to flow and the voltage drop decreases to zero. Similarly, when the MOSFET is switched off, the current reduces to zero and the voltage drop increases to its maximum value. During the delay, as the voltage drop increases or decreases, there is still some current and as such some power loss: $P_{S2} = \frac{1}{2} V_{DS} I \times f$. Here, the power loss of P_{S2} is also a function of frequency. The overall power loss in the MOSFET is the sum of the three types of power losses. After an evaluation, the IRF150 power MOSFET is selected due to its suitable ratings for this design.

The diode is one of the components of the MPPT with the highest power loss. The power loss is mainly due to the forward voltage drop of the diode, which can be significant for some diodes. The forward voltage drop is the voltage required before the diode is turned on and current is allowed to flow. The Schottky diode has the lowest on voltage (0.2 – 0.9V) when compared to other silicon general purpose and fast recovery diodes (0.7 – 2.5 V). There is a trade-off between the recovery speed, the breakdown voltage and the forward voltage drop. In our case, the lower forward voltage drop is preferable to the fast recovery speed and therefore the Schottky diode is suitable for the design.

Another component whose power loss varies as a function of frequency is the inductor. All inductors have some internal resistance, and the power loss is due to this resistance. Hence, the lower the internal resistance of an inductor, the lower the power loss will be. The internal resistance varies inversely with the wire gauge [21]; i.e. as the wire gauge increases, the internal resistance decreases. In general, a bigger inductor will have less internal resistance than a smaller inductor as more current passes through the bigger inductor. The drawback is the size and cost of the bigger inductor. Therefore, when selecting an appropriate inductor, it is important to strike a balance between a low internal resistance and the size and cost of a bigger inductor.

The power loss associated with the capacitor is similar to what obtains in the inductor. The parasitic series resistance causes heat to be dissipated resulting in power loss. When choosing the appropriate capacitor, a lower equivalent series resistance (ESR) should result in lower power loss. However, if the ESR is too low, arcing or welding can occur at the contacts, especially for non-solid state capacitors.

4.2 Voltage Sensing

Voltage measurements are required at several points in the circuit, particularly at the solar module output, and at the buck converter output. At the PV output, the voltage is measured with no current flowing to determine the open circuit voltage of the PV module. A fraction (80%) of the open circuit voltage is then used to determine the maximum power point voltage. Another point where the voltage measurement is required is the output of the first stage of the buck converter. The voltage at this point is the maximum power point voltage of the PV module. This desired MPP voltage is compared to the measured voltage and the difference is fed into an error amplifier that controls the PWM to achieve the necessary duty cycle needed to control the MOSFET switch.

The voltage at the output of the first stage of the converter is also the input voltage to the second stage of the converter. A measurement of the voltage at the output of the second stage of the buck converter is required to adjust the error amplifier and PWM to control the duty cycle, which then matches the desired load voltage. These voltage measurements are continuously collected and used in a dynamic feedback loop to maintain the solar module output and the load voltage at the desired levels. The voltage measurements can be achieved with the use of a high-impedance voltage sensing circuit [22].

4.3 Current Sensing

To measure the current through certain elements in the circuit, a small precision resistance (0.01Ω) connected in series with the elements can be used. The voltage drop across the resistor is directly proportional to the current through the element. The current measurements are necessary to ensure that the current through each element is within the device rating and the current supplied to the load is within the safe operating area of the load. The current measurements are particularly important in determining the power loss due to each element. In PSpice, the measurements are achieved by using the PROBE function of the software.

4.4 Testing and Verification

The circuit models of the solar cell and the maximum point power tracker have been simulated in PSpice. The solar cell and MPPT models must closely match the actual solar cell and desired operation of the MPPT so as to be able to accurately predict the performance of the system under varying atmospheric and load conditions. The circuit model of the solar cell is used to evaluate the effect of varying irradiation and temperature conditions on the output of the PV module. The MPPT circuit model is used to evaluate the effect of a feedback loop in the operation of the PV system.

4.4.1 Validation of PV Model

The PV panel is modeled as described in Section 3.3.2, using the electrical characteristics of the Sharp NE-80EJEA provided by the manufacturer's datasheet. The open circuit voltage is 21.6V while the short circuit current is 5.16A. The maximum power delivered is 80W, and the maximum power voltage and current occur at 17.3V and 4.63A respectively. The PV module is initially modeled under varying irradiation conditions with the solar cell temperature set to 25ºC. The I-V characteristic of the solar cell for irradiance values of 600, 800, and 1000 W/ m^2 are is shown in Fig. 4.1.

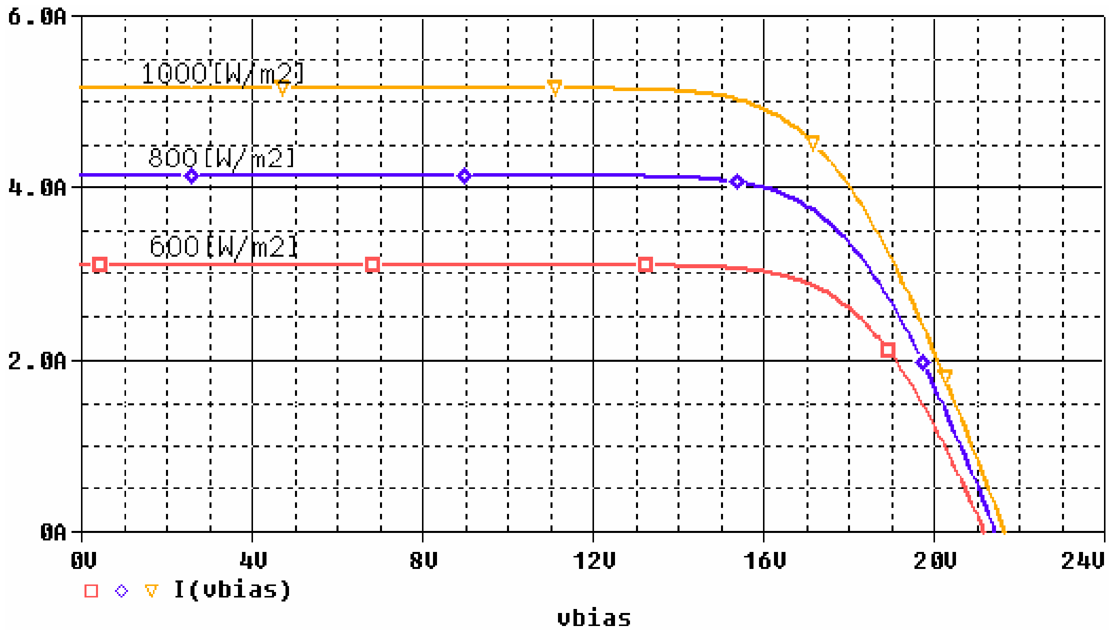

Fig 4.1: I-V characteristic at 600, 800, 1000 W/m^2 irradiation levels

Operating temperature affects the electrical output of the solar module. The I-V characteristic with varying operating temperature is shown in Figure 4.2. The module is set to operate with an irradiance value of 1000 W/ m^2. The operating temperatures are set at 20ºC, 25ºC, 40ºC, and 55ºC. The x-axis is the module's voltage while the y-axis is the module's current.

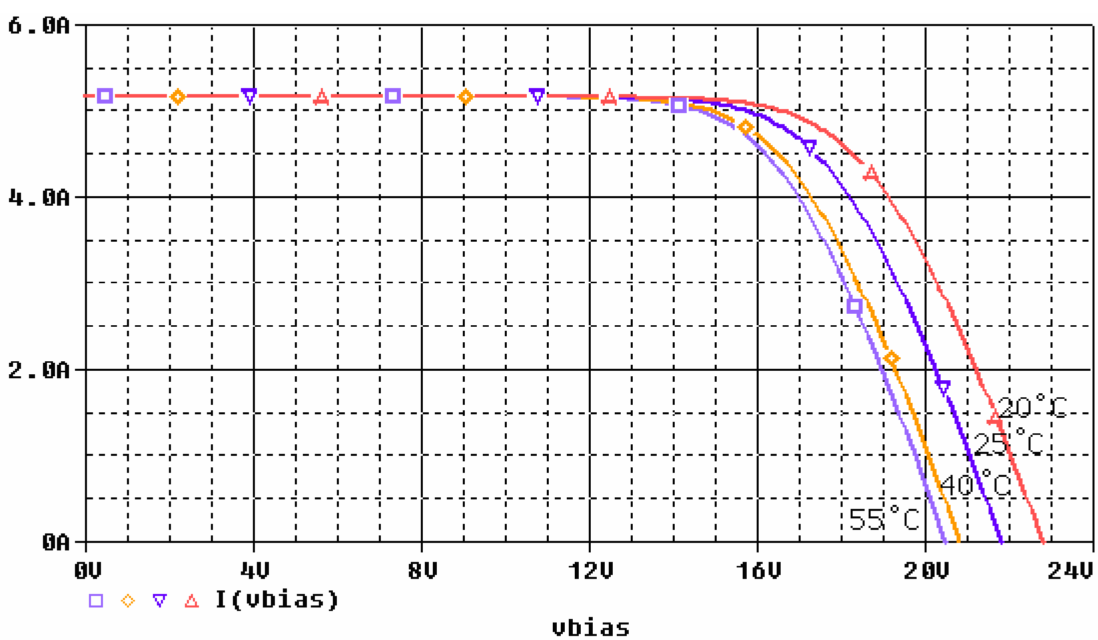

Fig 4.2: I-V characteristic at 20ºC, 25ºC, 40ºC, and 55ºC operating temperature

It should be noted that the short circuit current of the cell depends linearly on irradiation while the open circuit voltage depends logarithmically on irradiation. Therefore it would seem that the output voltage should increase as the irradiation level increases. However this is not necessarily so, since the cell temperature is likely to rise as the irradiation level increases. As discussed in chapter 2, an increase in cell temperature will generally lead to a reduction of the output voltage. This makes it imperative to consider the effect of temperature on the cell output voltage as illustrated in Fig. 4.2. Overall, there is a reduction of the voltage at higher irradiances due to the accompanying higher cell temperature [23]. A reduction in the terminal voltage or current will lead to a decrease in the output power since both the voltage and current are directly proportional to the output power, $P = V \times I$. The effect of irradiance and temperature on the output power of the solar cell is shown in Fig. 4.3 and Fig. 4.4.

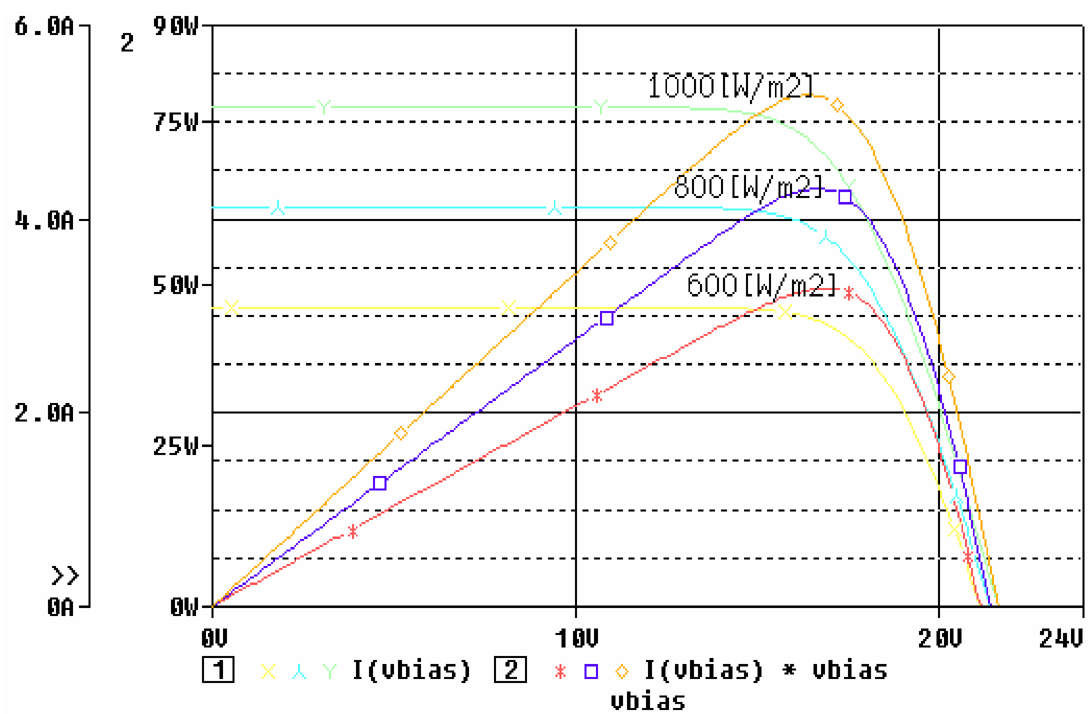

Fig 4.3: Output power at 600, 800, 1000 W/m^2 irradiation levels

The solar cell terminal voltage is located on the x-axis while the module's current and output power are located on the y-axis.

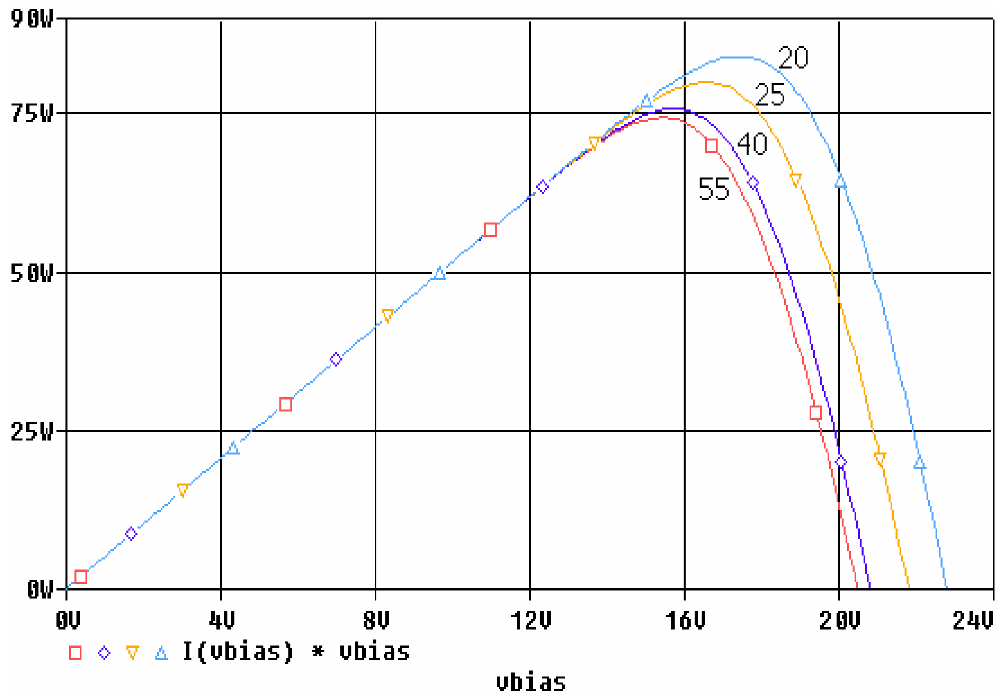

Fig 4.4: Output power at 20ºC, 25ºC, 40ºC, and 55ºC operating temp

The PV model's I-V characteristic closely matches the I-V characteristic provided in the manufacturer's data sheet and shown in Figure 3.5. The effect of decreasing irradiation level is demonstrated. It mostly affects the module's current and has only a slight effect on the module's voltage. The effect is greater on the module's current since the current decreases linearly with decreasing irradiance while the module's voltage only decrease logarithmically with decreasing irradiance. It is also observed that an increase in the operating temperature of the module has a reducing effect on the output voltage. Increasing module temperature causes a reduction of the output voltage and thus the output power of the solar module. If the temperature rises too much the cell may also be damaged by 'hot spots' [24].

4.4.2 Experimental Data

The example solar module was setup in the lab to verify the manufacturer's data and observe the effect of irradiance and temperature on the module's output voltage and current. The example solar module is shown in Fig. 4.5. The experimental setup involved measuring the output voltage and current under various illumination conditions.

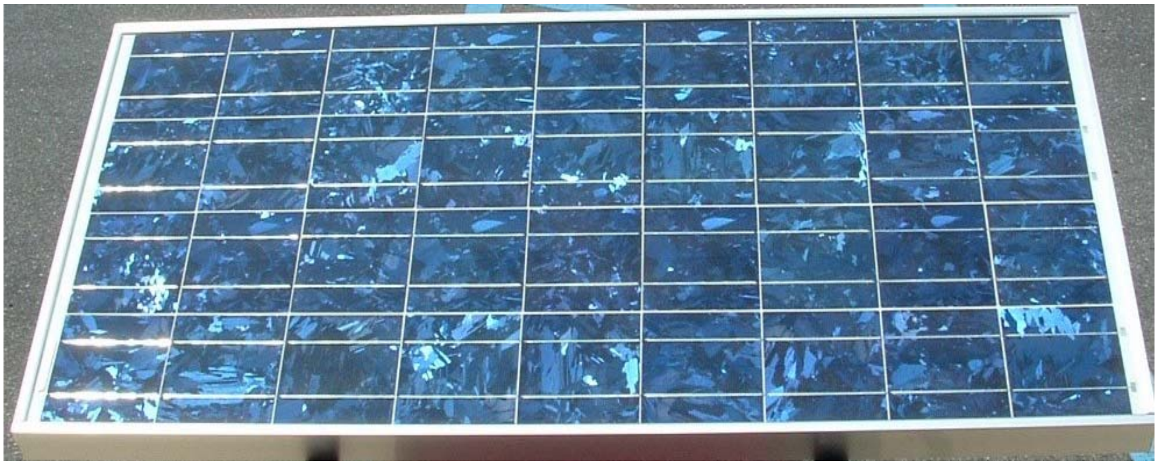

Fig 4.5: Sharp NE-80EJEA solar module used in experiment

The experiment was performed in both indoor and outdoor environments. The outdoors setup involved taking measurements under bright sunshine, slightly cloudy and very cloudy conditions. This allows for the observation of the solar module's response to varying irradiance levels. The indoor setup involved taking measurements under two artificial lighting conditions. The artificial lighting was achieved by using the laboratory's fluorescent lighting and an incandescent lamp. The different ambient temperature between the outdoor setup and the indoor setup allows for the observation of the module's response to varying temperature conditions. The results are presented in Tables 4.1 and 4.2.

Table 4.1:

Solar module measurements outdoor conditions:

Load Resistance **(Ω)**	Temp. **(°C)**	Bright Sunshine Output Voltage **(V)**	Slightly Cloudy Output Voltage **(V)**	Very Cloudy Output Voltage **(V)**	Partial Shadow Output Voltage **(V)**
∞ (V_{oc})	41.5	19.54	17.81	8.00	18.4
4.9	41.5	18.7	17.44	4.14	13.6
10.5	41	18.6	16.14	7.64	11.2
17	40	18.1	16.06	6.40	14.4

Table 4.2:

Solar module measurements under indoor conditions:

Load Resistance (Ω)	Temp. (°C)	Fluorescent Light Output Voltage (V)	Incandescent Lamp Output Voltage (V)
∞ (V_{oc})	25	7.83	13.75

As predicted from the PV model derived in chapter 3, the general trend for the solar module used in the experiment is a decrease in the output voltage and current as the module's exposure to the sun is reduced due to the presence of clouds. The output voltage is highest under bright sunshine and the output decreases under very cloudy conditions to less than half the output under bright conditions. The difference between the measured open circuit output voltage (19.54 V) and the manufacturer's specified open circuit voltage (21.6 V) may be attributed to the higher module temperature of 41.5 °C in the outdoor environment of our test case. The effect of partial shadow on the output voltage is also investigated and it is observed that a partial shadow on any part of the solar module will lead to a reduction of the output voltage.

The experiment was also performed under indoor conditions where the ambient temperature is 25 °C, the same temperature as the manufacturer's test conditions. The illumination indoors was significantly less than the illumination outdoors, but the output voltage in both indoor illumination conditions is higher than the output voltage under very cloudy outdoor conditions. The much lower indoor module temperature may be responsible for this and it demonstrates that higher irradiation levels do not necessarily lead to a higher output voltage because of the accompanying increase in temperature.

CHAPTER 5

Validation of MPPT Circuit Operation and Optimization

5.1 Validation of MPPT Circuit Modeling and Operation

The function of the MPPT is to maintain the output voltage of the solar module at it maximum power point regardless of variations in load demand. The MPPT also includes a second voltage regulation stage that maintains a steady output regardless of variations in the load demand. The validation of the MPPT circuit modeling and operation is performed in two stages: first the MPPT will be simulated with varying solar module output voltage, and then it will be verified via digital simulation by varying the load conditions.

For the first stage the supply's output voltage is at the maximum power point voltage of the solar module which was estimated earlier at 17.3V. For ease of simulation the output voltage of the solar module is assumed to be discrete DC voltages ranging from the open circuit voltage (21.6V) to 75% of the open circuit voltage (16V). The simulation results for the first stage of the MPPT at different input voltages are shown in Figures 5.1, 5.2, 5.3 and 5.4.

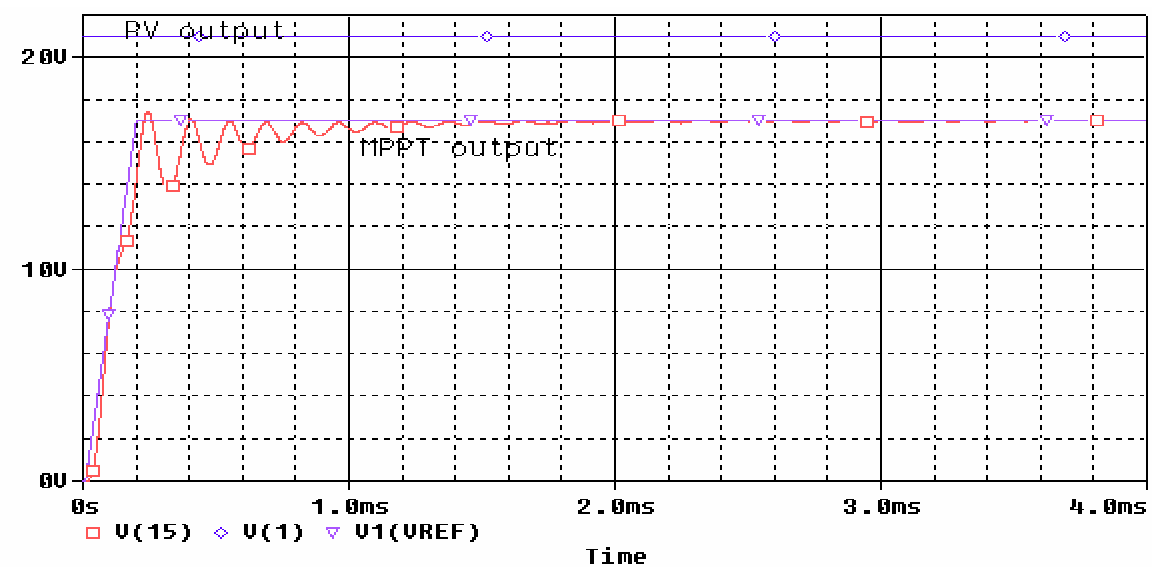

Fig 5.1: 1st stage of MPPT operating at 17.3V with PV output at 21V

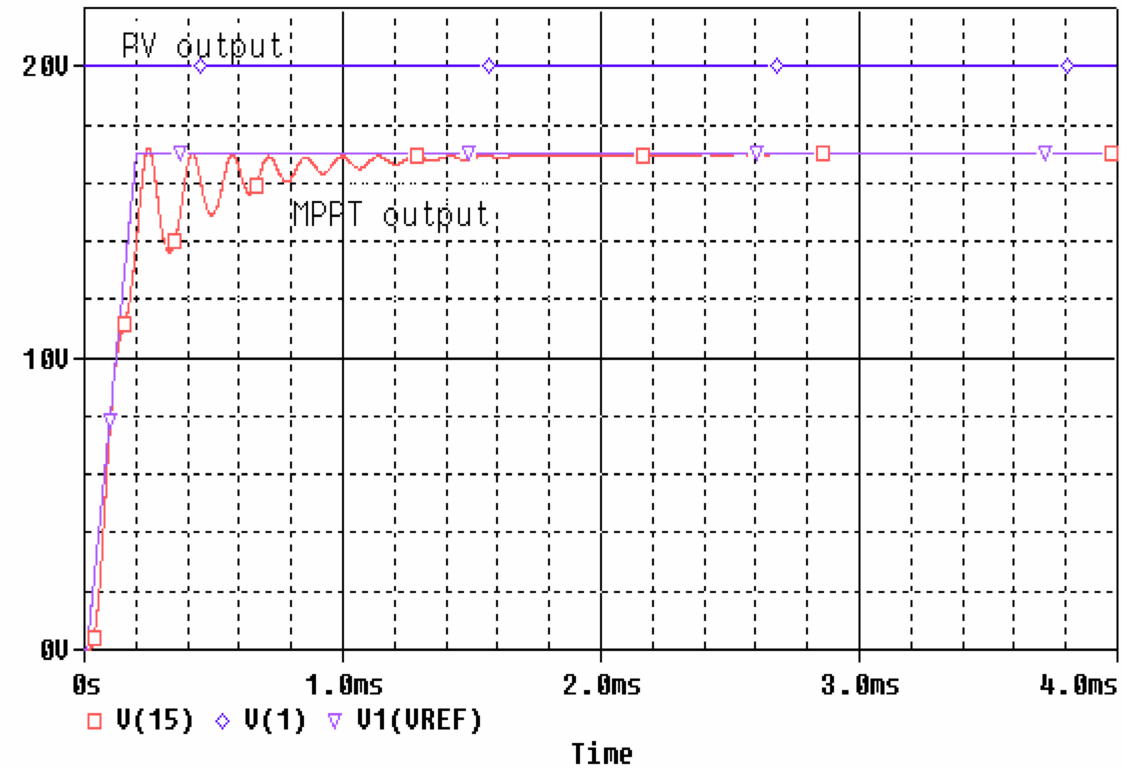

Fig 5.2: 1st stage of MPPT operating at 17.3V with PV output at 20V

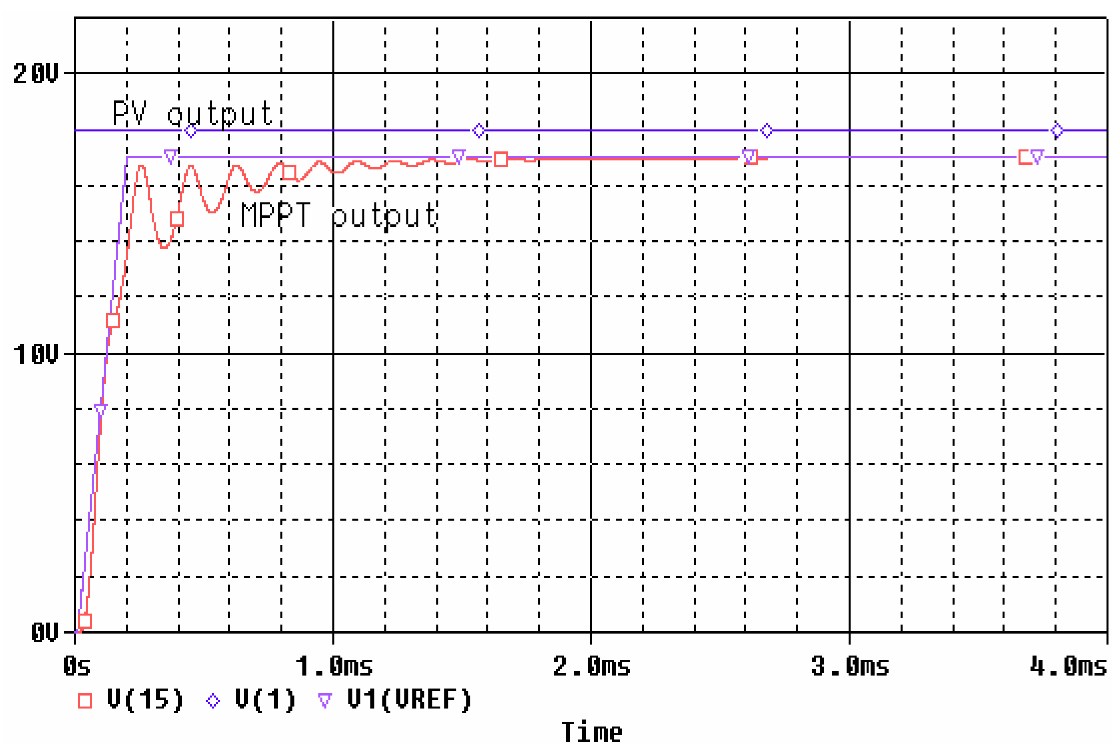

Fig 5.3: 1st stage of MPPT operating at 17.3V with PV output at 18V

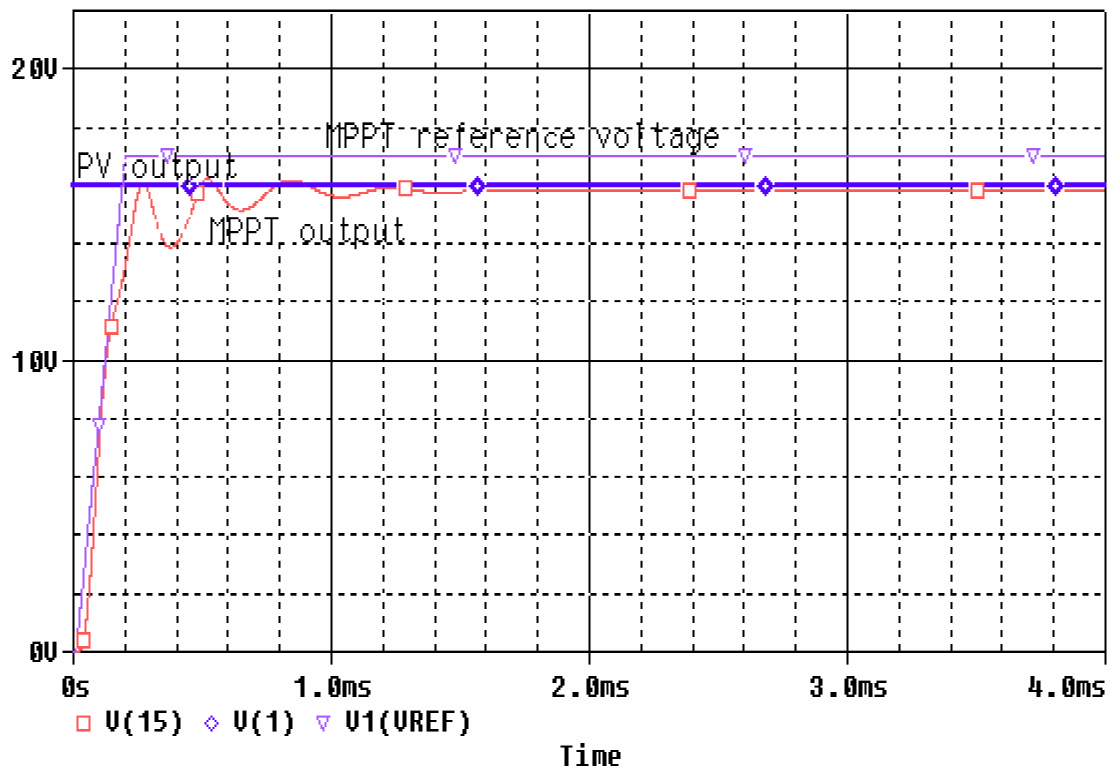

Fig 5.4: 1st stage of MPPT operating at 15.9V with PV output at 16V

As shown in Fig. 5.1 – 5.4, for the first three simulations with the PV output voltage greater than 17.3V, the MPPT is able to maintain the output at the maximum power point of 17.3V. However in Figure 5.4, where the PV output voltage is only 16V the MPPT can only sustain an output voltage equal to the output voltage of the PV module. This is somewhat expected as the MPPT is of the buck converter type which is only able to output a voltage smaller than the input voltage. Therefore if the solar output falls below 17V due to temperature or atmospheric conditions, then the MPPT can only output a voltage equal to the voltage produced by the PV module.

Under normal operating conditions, with proper illumination, the PV module's output voltage is expected to vary only a couple of volts as temperature and irradiation conditions change [25]. Thus, the buck converter should work well for our design under most conditions. A more complex design of the MPPT implementing either the buck-boost or Cuk converter type [26] will solve the problem of low PV output voltage as both converter types can either reduce or increase the output voltage from a nominal input voltage.

The second stage of the MPPT is the output voltage regulation stage. The MPPT is able to maintain a constant charging voltage of 12V to the ultra-capacitor or battery regardless of changes in load conditions. A simulation of the second stage of the MPPT is shown below in Fig. 5.5.

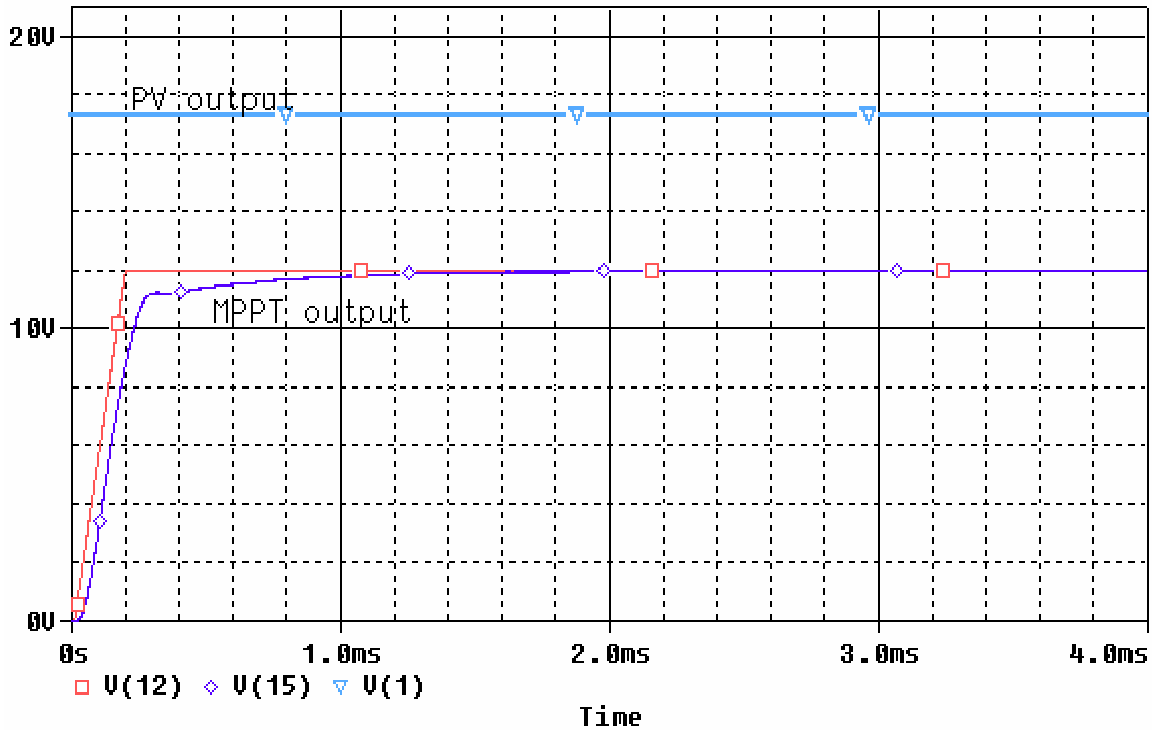

Fig 5.5: 2nd stage of MPPT with PV output at 17.3V and MPPT output at 12V

Now to check if the feedback loop can maintain the output voltage at the required 12V in steady-state that is required to charge the ultra-capacitor and/or battery bank. A transient load is applied to observe the tracking response of the MPPT against any load variation. The transient load is achieved by using a pulsed current source to add a 1A increase in load demand between 1.0 ms and 2.0 ms. A second simulation is performed with the pulsed load added between 2.5 ms and 3.5 ms. The results of the simulation are shown in Fig. 5.6 and 5.7, respectively.

From the simulation results of Fig. 5.6 and 5.7, it is observed that the designed MPPT in Fig. 3.16 is able to quickly adjust the output voltage to the desired output voltage of 12V even with the increase in load demand.

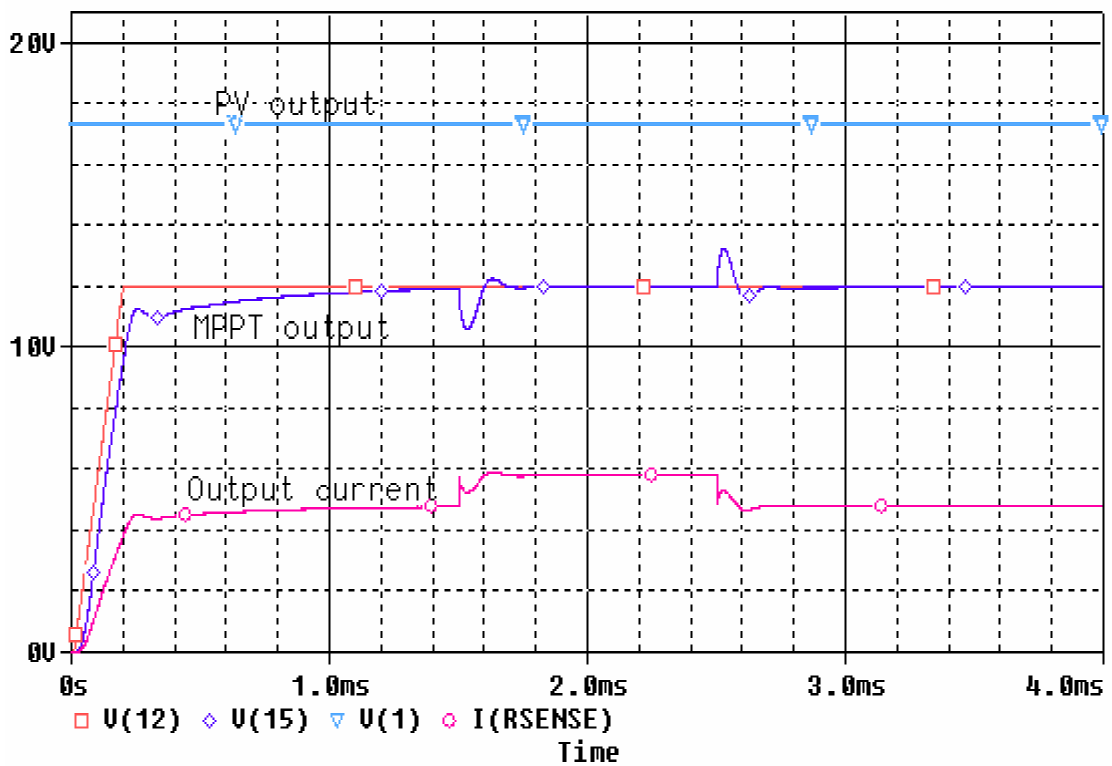

Fig 5.6: MPPT output voltage with pulsed load added between 1.5ms and 2.5ms

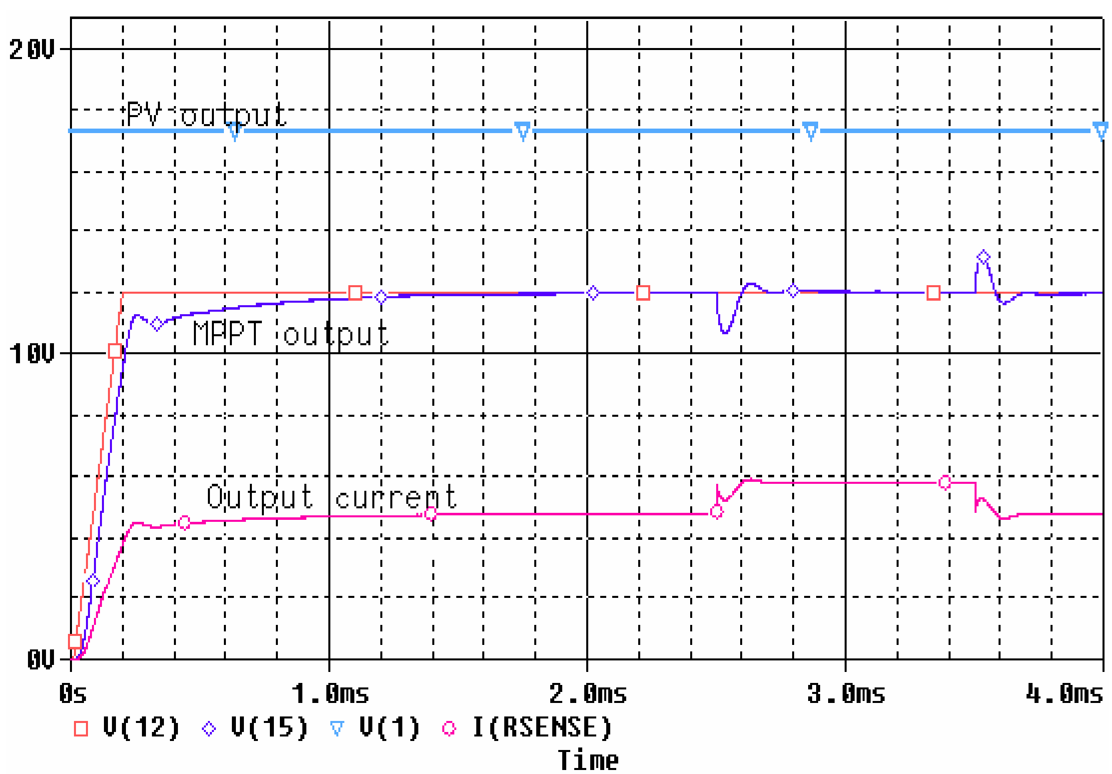

Fig 5.7: MPPT output voltage with pulsed load added between 2.5ms and 3.5ms

5.2 Control and Optimization using Microcontroller

In coming up with an MPPT design, one of the more important factors that was considered was the simplicity of the design. The goal was to model a simple MPPT that would effectively extract the most power from the PV module. The components used are readily available and the MPPT does not require a complex tracking mechanism. However, to further improve the control performance and increase the functionalities for general-purposed MRDEG systems, a low-cost microcontroller is preferred. A microcontroller can replace multiplying analog and digital components, such as the error amplifier circuit and the PWM circuit.

Most microcontrollers incorporate timers, PWM Input and Output, A/D and D/A interfaces, Interrupts for timing control and communications. They can also perform comparison functions. A simple microcontroller, the PIC16F873, has being evaluated and its features which include 8K x 14 bytes of flash memory, 368 x 8 bytes of RAM, five A/D and two D/A channels can be used to control a MPPT power circuit and tracking operation. The PIC16F873 offers a good balance of features, low cost and low power consumption. Key specifications and technical data are given in Appendix B. The use of a microcontroller provides more benefits as the MPPT operation can be enhanced by implementing a digital control strategy. An effective digital control strategy will better match the PV module's output to the maximum power point when compared to the analog control method [27].

5.3 Feedback Control using Microcontroller

In the case of a practical implementation, a feedback control loop is necessary to ensure proper operation of the maximum power tracking. The feedback loop is used to continuously adapt the maximum power point as temperature and load conditions vary. The feedback control also ensures the stability of the MPPT and prevents unsafe operating conditions of the PV module and the load. Several methods to control the operation of the MPPT have been proposed [28]. Two of the most widely used control methods are the voltage-feedback control and the power-feedback control.

For the voltage-feedback control, the solar panel terminal voltage is used as the control variable for the MPPT. This system keeps the solar panel operating close to its maximum power point by regulating the panel's voltage and matching the solar panel voltage to the desired voltage. The advantage of this approach is that no calculations are required in determining the panel's operating voltage and a simple op-amp circuit is sufficient to carry out the regulating and matching functions. However, the voltage-feedback control method has some limitations including neglecting the effect of temperature and insolation on the solar panel. Hence, this method is only suitable for use when the effects of insolation and temperature are minimal.

The other commonly used control method is the power-feedback control method. Here, the maximum power control is achieved by forcing the derivative of the output power against the terminal voltage $\left({dP}/{dV}\right)$ to be equal to zero [29]. The general approach is to measure and maximize the power at the load terminal by matching the change in power delivered to the change in output voltage. The advantage of the approach is that the maximum power can be delivered to the load without necessarily knowing the solar panel characteristics. However, this approach only maximizes the power delivered to the load and not the power extracted from the solar panel.

A combination of both the voltage-feedback control and the power- feedback control method results in a two-dimensional tracking strategy that maximizes the power extracted from the solar module and the power delivered to the load. To overcome the limitations of the voltage-feedback control method, wattage sampling techniques [30] are used to continuously find the solar panel's optimal operating voltage.

The wattage sampling technique involves periodically introducing a small change in the panel input voltage, measuring the current, and then calculating the input wattage. If the wattage has increased over the last sample, then the next change in the reference voltage should continue in the same direction. The next change in voltage would be in the opposite direction if the wattage had decreased over the previous sample. This method results in the PV voltage being dynamically adjusted to increase the output power. While the PV output voltage technically operates close to the actual maximum power point, it oscillates around the true peak point, and the error should be negligible. A flowchart of the control algorithm for the power-feedback control is shown in Fig. 5.8.

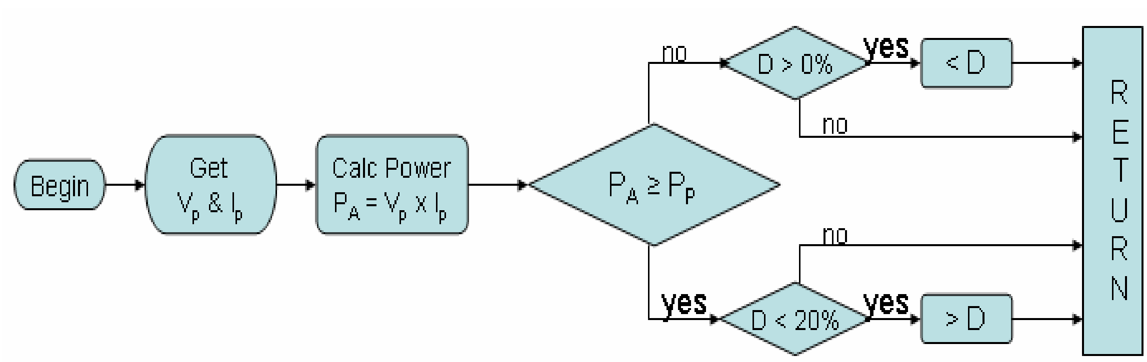

Fig 5.8: Flowchart of the power-feedback control algorithm

One of the ways of improving the MPPT performance is to optimize the amplitude of the duty cycle perturbation. Lowering the change in the duty cycle (ΔD) reduces the steady-state losses caused by the oscillation of the solar array operating point around the maximum power point [31]. However, reducing ΔD makes the algorithm less efficient under certain conditions. A lower ΔD means the algorithm is unable to quickly adjust to rapidly changing atmospheric conditions since it has to run through several iterations before arriving at the maximum power point.

Another parameter that affects the performance of the MPPT is the sampling interval used in the wattage sampling technique. The sampling interval must be properly set above a threshold value in order to avoid instability of the MPPT algorithm and to reduce the number of oscillations around the MPP in steady-state operation. The threshold value for the sampling interval takes into account the transient behavior of the whole PV system when sampling the array voltage and current. Thus, after each duty cycle perturbation, the system should reach steady-state before the next measurement of array voltage and current is performed.

5.4 Application of Artificial Neural Networks

Further optimization of the MPPT algorithm can be achieved and implemented by using artificial neural networks to predict the maximum power point of the solar array [32]. Steady-state losses are reduced by using smart approximation to predict the location of the maximum power point which reduces the number of iterations required to reach the MPP and minimizes the oscillation around the MPP.

Artificial neural networks (ANN) are electronic models based on the neural structure of the brain. The ANN mimics the function of the brain by ‘learning’ from experience. This function permits ANNs to be used in the design of adaptive and intelligent systems since they are able solve problems from previous examples. ANN models involve the creation of massively paralleled networks composed of mostly of nonlinear elements known as neurons. Each model involves the training of the paralleled networks to solve specific problems.

The ANN models work by associating an output value to each neuron, known as the neuron’s activation. A value called the synaptic weight is also associated with each connection between the neurons. The activation of each neuron then depends on the activations of the neurons connected to it and the interconnection weights. ANNs are simple clustering of neurons in layers, where the activations of the input layer are set by an external parameter. Most networks contain at least three layers – input, hidden, and output. The input layer receives data usually from an external source while the output layer sends information to an external device. There may be one of more hidden layers between the input and output layers. Artificial neural networks are defined by their network topologies, the features of their neurons, and by their training or learning algorithm [33].

5.4.1 Back-propagation

The most common type of learning algorithm is the back-propagation method. The back-propagation network is an example of a non-linear layered feed-forward network. The back-propagation network able to adapt by using a learning set consisting of some input examples and the known-correct output for each case to learn the expected behavior. The learning process works in small iterative steps as the learning set is applied to the network and the output produced based on the current synaptic weights is compared to the known-correct output and a mean-squared error is calculated. The error value is propagated back through the network and small adjustments are made to the weights in each layer. The process is repeated until the error value drops below some threshold value. At this point, the network has sufficiently learned the problem.

The back-propagation type of learning method is suitable for use in predicting the maximum power point of a solar array [34]. The algorithm is trained by using data collected from the solar array. The insolation, temperature and load voltage values are used as the activation values for the input layer of the network. The structure of the proposed back-propagation neural network is shown in Fig. 5.9. The network is fully connected meaning that the output of each neuron is connected to all neurons in the hidden layer through the synaptic weight. The weights are continuously updated through successive iterations until the error drops below the threshold value [34].

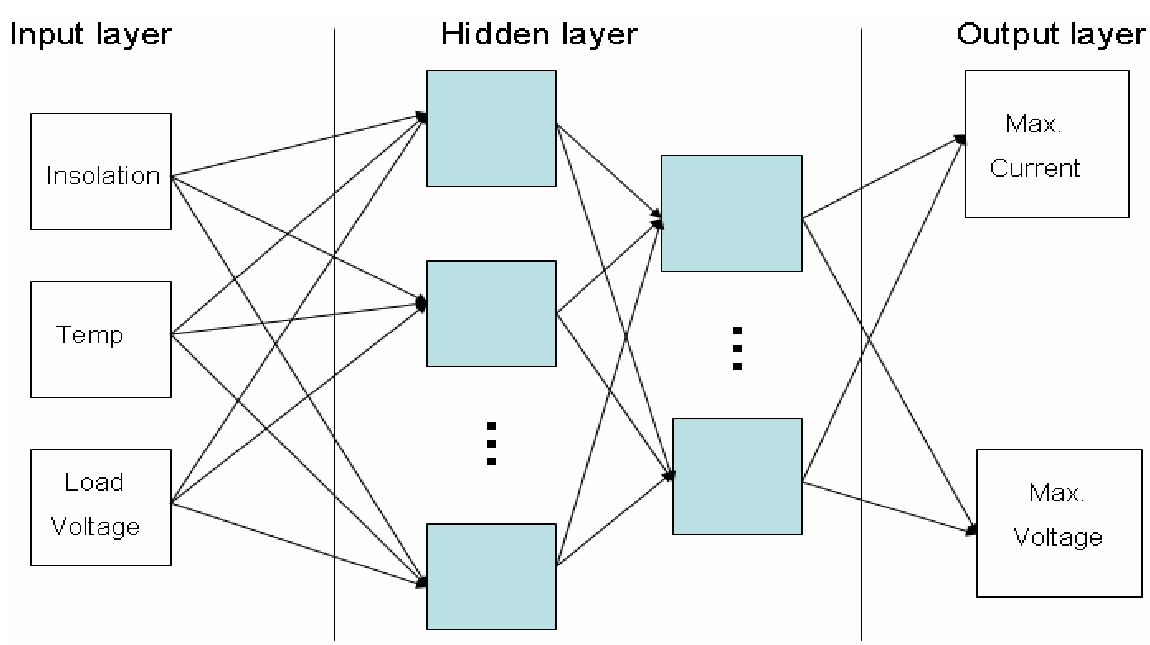

Fig 5.9: Structure of back-propagation neural network for maximum power tracking

The back-propagation algorithm is stored on the micro-controller while the insolation, temperature, and load voltage data are collected for each tracking cycle. The microcontroller uses the data as the activation input to run the back-propagation algorithm. Once the back-propagation neural network is trained the algorithm estimates the maximum power point voltage and current. This operating point is used as the starting position for determining the maximum power point using the wattage-sampling control method.

The Pseudo-code for the proposed back-propagation algorithm is described below:

- Initialize weight vector W to small random numbers for both layer transition
- Set constants and initialize variables
- Train algorithm by taking input vector and setting to target vector by setting appropriate learning rate
- Create values at hidden and output nodes
- Create deltas first at the output nodes and then at the hidden nodes
- Update the weights
- Compute the sum-squared error and the average error
- Repeat until termination condition is met

The solar array voltage and current are at the maximum power point when the error is below the threshold value. An appropriate learning rate is selected by adjusting the change in error and the array operating point. A gradient descent minimization can be performed on the error function to smooth the learning rate [35].

CHAPTER 6

Conclusion and Future Work

6.1 Conclusion

The aim of this research work is to develop a method to optimize the energy extraction from a proposed renewable energy generation system. In order to achieve this, the components and subsystems have to be analyzed and validated. The validated models can then be used to maximize the power output of the conversion system.

The photovoltaic model was modeled and validated in PSpice. The results of the simulation were compared to experimental data obtained in the lab and both results were found to be very close. The simulations showed the effects of irradiance and temperature on the operating condition of the photovoltaic module. The simulation results showed that an increase in irradiance generally caused an increase in the module's output current while an increase in operating temperature generally caused a drop in the module's terminal voltage. In fact, the results showed a linear relationship between the short circuit current and the irradiance level while there is a logarithmic relationship between the open circuit voltage and the operating temperature.

An MPPT design was implemented and modeled in PSpice. The simulation results of the MPPT showed that the tracker was able to maintain the operating point of the photovoltaic module at the maximum power point thereby improving the amount of energy successfully extracted from the module. The MPPT also performed well as a charge regulator to the energy storage components.

The simulation results indicate that a significant amount of additional energy can be extracted from a photovoltaic array by using simple analog or digital maximum power point trackers. This results in improved efficiency for the operation of renewable energy generation systems. The improved efficiency should lead to significant cost savings in the long run.

6.2 Further Work

In the future, a more detailed model of the photovoltaic module can be developed from the one presented in this work. The more detailed model may take into account the effect of shading or partial shadows on the operation of the module. Also the effects of scaling up the photovoltaic sources may be investigated to determine the suitability for large scale deployment.

Different algorithms for maximum power control can be developed for application on other renewable energy sources such as fuel cells and wind power. Artificial neural network algorithms can be developed to improve the performance of the solar energy conversion function of the MPPT. Overall, the shift from conventional energy sources to alternative energy means a lot more work needs to be done to fulfill the desire to produce clean, affordable and sustainable energy.

APPENDIX A (Components and Subsystems)

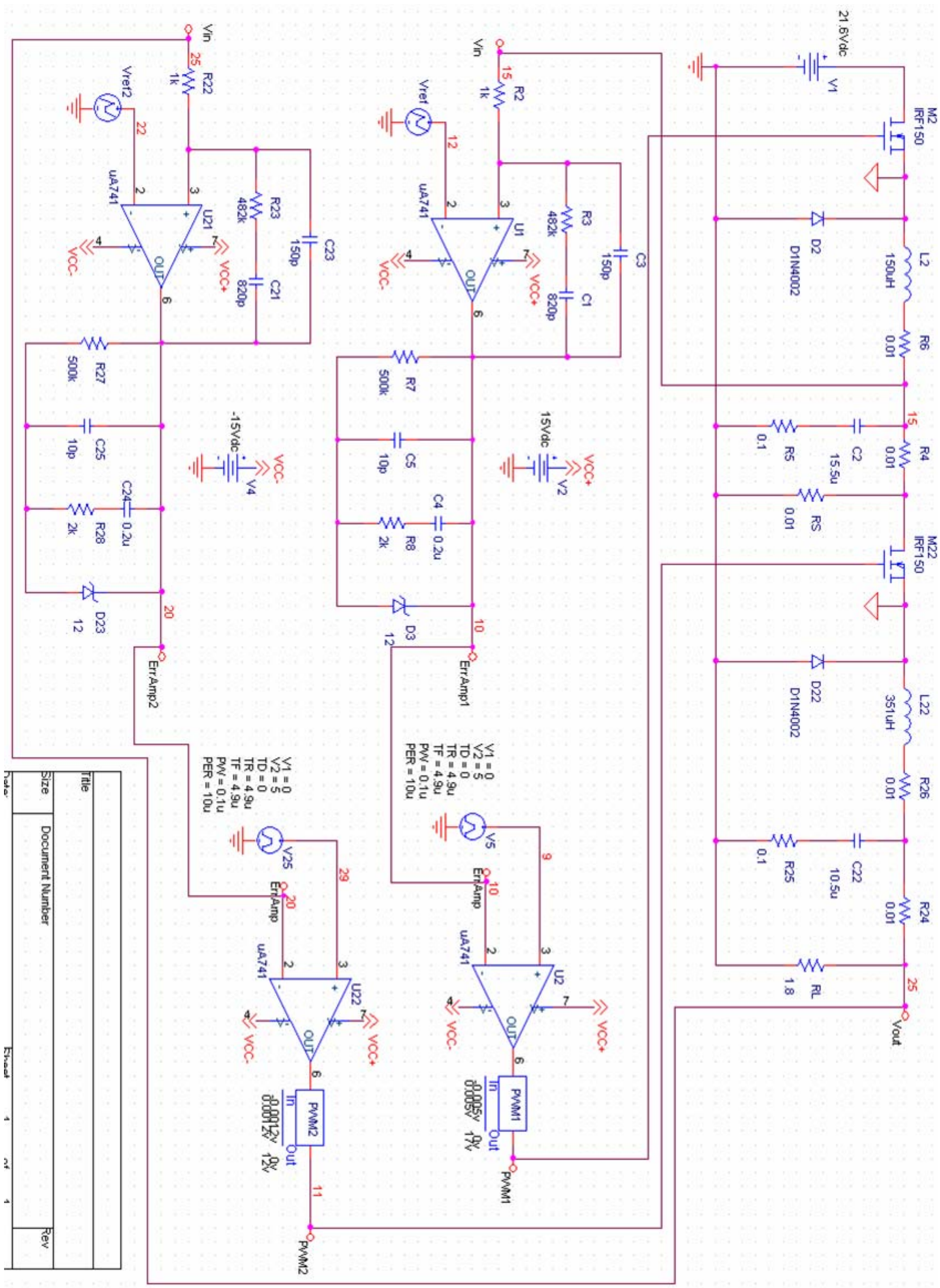

Figure A-1: MPPT Circuit PSpice Schematic

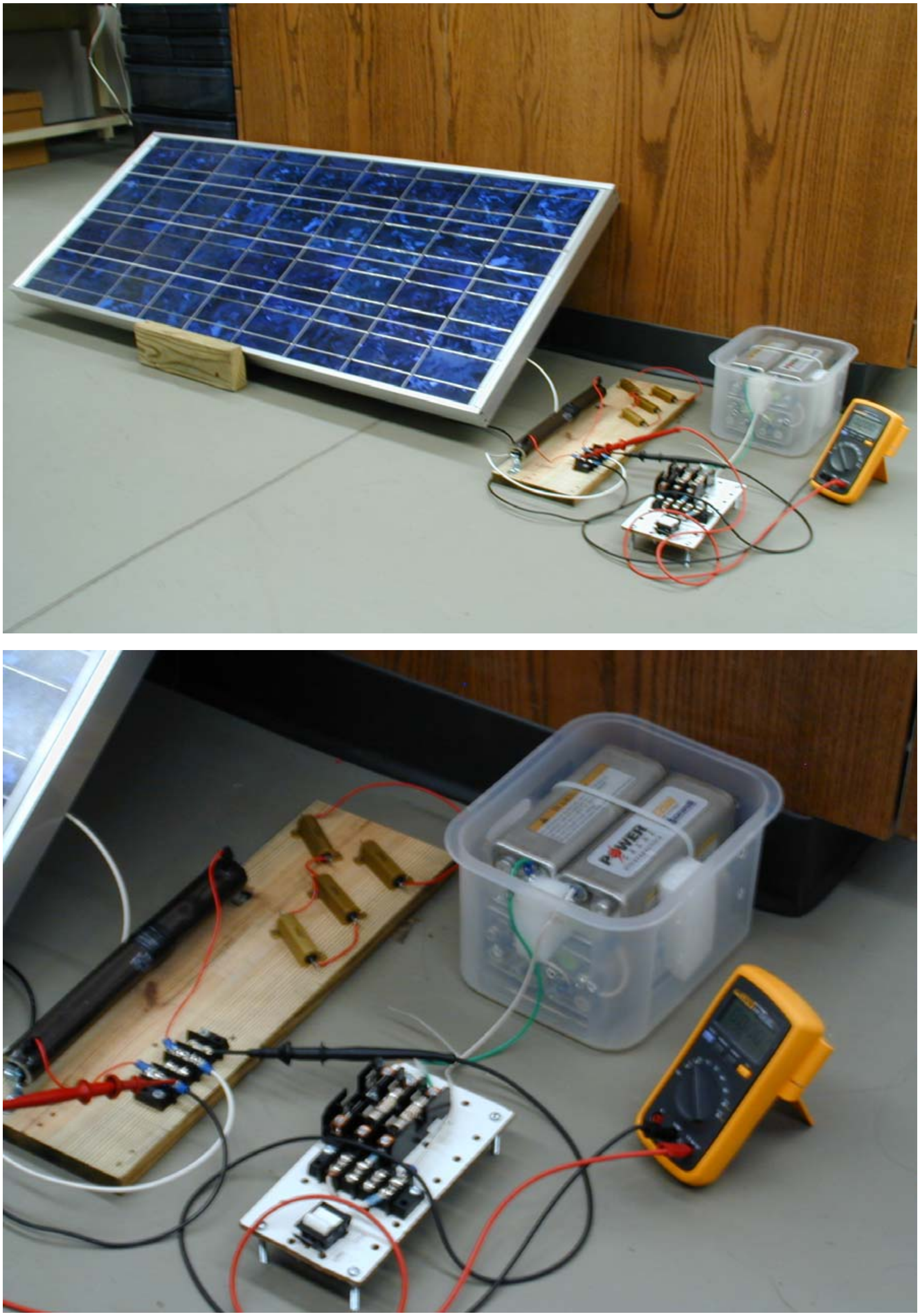

Figure A-2: Experimental setup for solar module under indoor conditions

NE-80EJEA

MULTI-PURPOSE MODULE

80 WATT

ELECTRICAL CHARACTERISTICS

Cell	Poly-crystalline silicon
No. of Cells and Connections	36 in series
Open Circuit Voltage (Voc)	21.6V
Maximum Power Voltage (Vpm)	17.3V
Short Circuit Current (Isc)	5.16A
Maximum Power Current (Ipm)	4.63A
Maximum Power (Pmax)*	80W (+10% / -5%)
Module Efficiency (ηm)	12.40%
Maximum System Voltage	600VDC
Series Fuse Rating	10A
Type of Output Terminal	Junction Box

* (STC) Standard Test Conditions: 25°C, 1 kW/m², AM 1.5

MECHANICAL CHARACTERISTICS

Dimensions (A x B x C)	47.28" x 21.14" x 1.81" 1200mm x 537mm x 46mm
Weight	20.94lbs / 9.5kg
Packing Configuration	1 pc per carton
Size of Carton	53.15" x 27.56" x 2.95" 1350mm x 700mm x 75mm
Loading Capacity (20 ft container)	242 pcs (242 cartons)
Loading Capacity (48 ft container)	506 pcs (506 cartons)

ABSOLUTE MAXIMUM RATINGS

Operating Temperature	-40 to +194°F / -40 to +90°C
Storage Temperature	-40 to +194°F / -40 to +90°C

IV CURVES

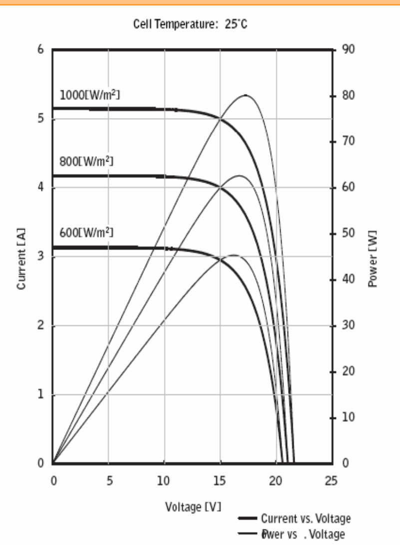

Current, Power vs. Voltage Characteristics

DIMENSIONS

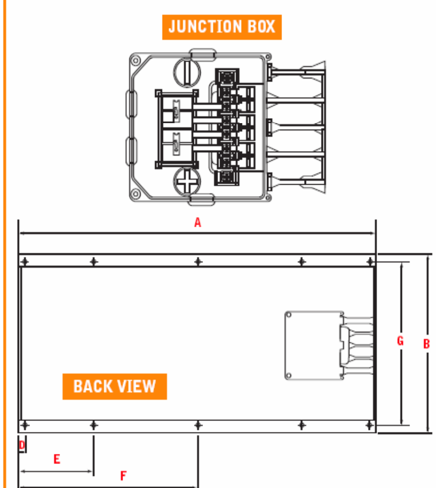

A	B	C	
47.28"/1200mm	21.14"/537.1mm	1.81"/46mm	
D	**E**	**F**	**G**
.99"/25.1mm	9.84"/250.0mm	23.62"/600.0mm	18.9"/480.0mm

Design and specifications are subject to change without notice.

In the absence of confirmation by product manuals, Sharp takes no responsibility for any defects that may occur in equipment using any Sharp devices.
Contact Sharp to obtain the latest product manuals before using any Sharp device.

SHARP

Sharp Electronics Corporation • 5901 Bolsa Avenue, Huntington Beach, CA 92647
Tel:1-800-SOLAR-06 • E-mail: sharpsolar@sharpusa.com • www.sharpusa.com/solar

Cover photo: Solar installation by Hudson Valley Clean Energy, Rhinebeck NY   SSD-80-606

Figure A-3: Sharp NE-80EJEA Solar Cell Data Sheet

IFCS1200-200509-C

FCS 1200™

How It Works

The FCS 1200™ is a self-contained fuel cell system. Hydrogen is generated by IdaTech's onboard FPM 20™ fuel processor. The processor uses fuel from an onboard tank and ambient air to convert liquid fuel into high-purity hydrogen using metal membrane purification technology. High-purity hydrogen is then delivered to the anode side of the PEM fuel cell stack. Inside the fuel cell stack electrons are separated from the hydrogen creating a hydrogen ion. The ion passes through the proton exchange membrane (PEM) where electrons are stripped, collected and delivered to connected loads as electricity. The hydrogen ion, the stripped electrons and ambient oxygen combine at the cathode side to produce the only system emission–warm water vapor. Electricity is generated at the fuel cell stack as direct current (DC). An optional pure sine wave inverter converts the DC electricity into high quality alternating current (AC) electricity if desired.

The IdaTech FCS 1200™ fully integrated fuel cell system is the most compact complete system available.

The FCS 1200™ is currently being tested in a Solar-Fuel Cell Hybrid application.

Common Specifications:

Fuel:	Methanol/De-Ionized water mix
Fuel Mix Consumption (@ 1 kW):	1.4 Liters/hr
Fuel Mix Consumption (idle):	0.2 Liters/hr
Fuel Capacity:	11.2 Liters
Sound Level:	<55 dB @ 1 meter
Dimensions (LxWxH):	74 x 69 x 64 cm; 29″ x 27″ x 25″
Weight (varies w/options):	77-84 kg; 170-185 lbs.
Operating Temperature:	3 to 30° C
Storage Temperature:	-20 to 50° C
Exhaust Temperature:	<50° C
Ventilation Requirement (indoor use):	70 Liters / sec

AC Model Specifications:*

Continuous Output Power:	850 Watts (120 VAC or 240 VAC) True Sine Output
Peak Output Power (10 sec.):	2000 Watts
Voltage Output:	120 VAC, +/- 5%, 60 HZ +/- 0.1% or 240 VAC +/- 5%, 50 Hz +/- 0.1%

DC Model Specifications:**

Continuous Output Power:	1000 Watts (48 VDC nominal)
Peak Output Power (1 min.):	2000 Watts (48 VDC nominal)
Voltage Range:	44.0 - 56.0 VDC

* AC de-rating specifications are 17 W/100 meters & 17 W/deg C >30
**DC de-rating specifications are 15 W/100 meters & 15 W/deg C >30

Powered by BALLARD™

IDATECH®
An IDACORP Company
Advanced Fuel Cell Solutions℠

63065 N.E. 18th Street • Bend, Oregon 97701 • Phone: (541) 383-3390 • Fax: (541) 383-3439 • www.idatech.com • info@idatech.com

Figure A-4: IdaTech FCS 1200 Fuel Cell Data Sheet

Maxwell TECHNOLOGIES

Electric Double Layer Capacitor: BOOSTCAP® Ultracapacitor

Square, bus bar type

Series: PC2500

BOOSTCAP® ULTRACAPACITORS

› Features:

- Over 500,000 duty cycles
- 10 year life capability
- Higher energy vs electrolytic
- Higher power vs. batteries
- Aluminum construction

› Applications:

- Automotive subsystems
- Wireless transmissions

› Dimensions:

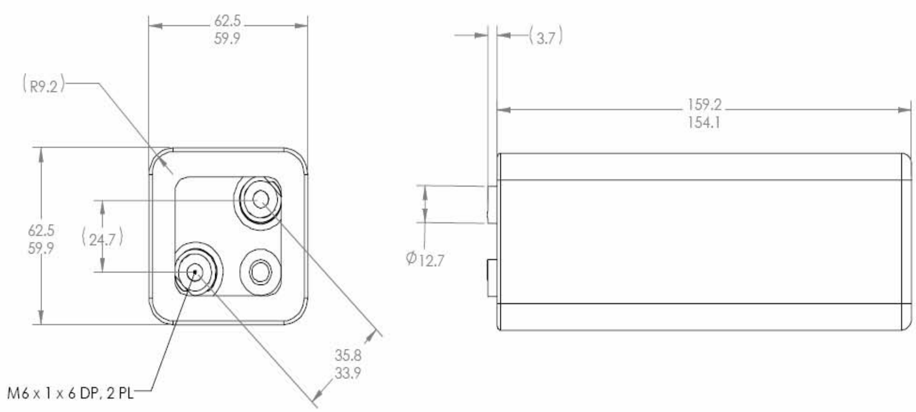

Case size	Dimensions, mm L	W	T	Weight [g]	Vol. [l]	Typical package qty
PC2500	161	61.5	61.5	725	0.6	25

**NOTE: PC2500 available in limited quantity only.
The MC2600 is the replacement part for this product.
Please contact BOOSTCAP Sales for additional information.**

Product dimensions and specifications may change without notice. Please contact Maxwell Technologies directly for any technical specifications critical to application.

Electric Double Layer Capacitor: BOOSTCAP® Ultracapacitor | Doc. # 1003992 | Rev. 5 |

Figure A-5: Maxwell BOOSTCAP Ultracapacitor Data Sheet

› Specifications:

NOTE: PC2500 available in limited quantity only.

	Product Specification		
	PC2500	Tolerance	Standard
Mounting	Bus Bar		
Capacitance, C_R [F]	2,700	+/- 20%	
Voltage, U_R	2.5		
Internal resistance, DC [ohm]	0.001	+/- 25 %	
Internal resistance, 1 kHz [ohm]	0.00055	+/- 25 %	
Rated current, [A]	100		5s discharge to 1/2 U_R
Short circuit current, I_{sc} [A]	4500		**Caution**, current possible with short circuit from U_R
Leakage current [mA]	6		72 hrs, 25°C
Operating temp. range [C]	-40 to 65		
Storage temp. range [C]	-40 to 85		
Endurance, Capacitance [F]	< 20% decrease		1000 hrs @ U_R and 70°C
Endurance, Resistance [ohm]	< 40% increase		
Maximum energy, E_{max} [mAh]	1,800		Full discharge from U_R
Power, P_d [W/kg]	1,030		See additional technical information
Power, P_v [W/l]	1,250		See additional technical information
Life Time	△C < 20% decrease, ESR < 200% increase		from initial value after 10y @ 25°C
Cycle Life	△C < 20% decrease, ESR < 200% increase		from initial value after 500K cycles @ 25°C (I = 20A)

› Markings: Capacitors are marked with the following information

Rated capacitance, Rated voltage, product number, name of manufacturer, positive and negative terminal, warning marking.

› Mounting Recommendations:

Component to be mounted with bus bar rated for application current. Maximum torque recommendation is 60 inch lbs. Use of lock washer recommended. See Integration Kit for additional recommendations.

Components should not be operated outside recommended limits.

› Additional Technical Information:

$P_d = (0.12 \times E^2/R_d)/M$ where E = charge voltage (U_R), R_d = internal resistance (DC)
M = capacitor weight (kg)

$P_V = (0.12 \times E^2/R_d)/V$ where V = capacitor volume (l)

US Patents: 6,430,031; 6,233,135; 5,907,472; 5,862,035; 5,777,428; 5,621,607

Worldwide Headquarters
MAXWELL TECHNOLOGIES
9244 Balboa Avenue • San Diego, 92123 CA, USA
PHONE: +(1) 858 503 3300
FAX: +(1) 858 503 3301
EMAIL: info@maxwell.com

European Office
MAXWELL TECHNOLOGIES SA
CH-1728 Rossens • Switzerland
PHONE: +41 (0) 26 411 85 00
FAX: +41 (0) 26 411 85 05
EMAIL: info@maxwell.com

www.maxwell.com

Figure A-5(b): Maxwell BOOSTCAP Ultracapacitor Data Sheet

APPENDIX B (Microcontroller)

MICROCHIP

PIC16F87X

28/40-Pin 8-Bit CMOS FLASH Microcontrollers

Devices Included in this Data Sheet:

- PIC16F873
- PIC16F874
- PIC16F876
- PIC16F877

Microcontroller Core Features:

- High performance RISC CPU
- Only 35 single word instructions to learn
- All single cycle instructions except for program branches which are two cycle
- Operating speed: DC - 20 MHz clock input
  DC - 200 ns instruction cycle
- Up to 8K x 14 words of FLASH Program Memory,
  Up to 368 x 8 bytes of Data Memory (RAM)
  Up to 256 x 8 bytes of EEPROM Data Memory
- Pinout compatible to the PIC16C73B/74B/76/77
- Interrupt capability (up to 14 sources)
- Eight level deep hardware stack
- Direct, indirect and relative addressing modes
- Power-on Reset (POR)
- Power-up Timer (PWRT) and Oscillator Start-up Timer (OST)
- Watchdog Timer (WDT) with its own on-chip RC oscillator for reliable operation
- Programmable code protection
- Power saving SLEEP mode
- Selectable oscillator options
- Low power, high speed CMOS FLASH/EEPROM technology
- Fully static design
- In-Circuit Serial Programming™ (ICSP) via two pins
- Single 5V In-Circuit Serial Programming capability
- In-Circuit Debugging via two pins
- Processor read/write access to program memory
- Wide operating voltage range: 2.0V to 5.5V
- High Sink/Source Current: 25 mA
- Commercial, Industrial and Extended temperature ranges
- Low-power consumption:
  - < 0.6 mA typical @ 3V, 4 MHz
  - 20 µA typical @ 3V, 32 kHz
  - < 1 µA typical standby current

Pin Diagram

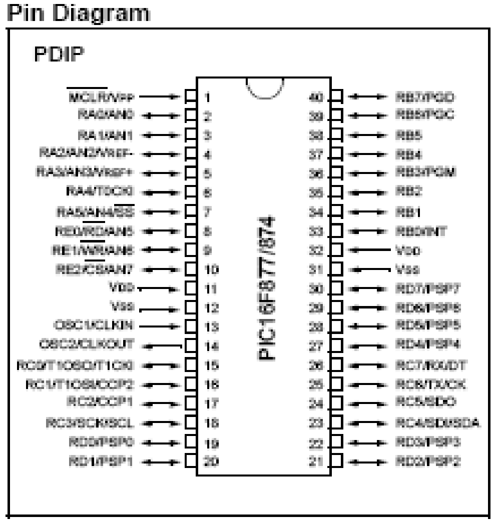

Peripheral Features:

- Timer0: 8-bit timer/counter with 8-bit prescaler
- Timer1: 16-bit timer/counter with prescaler, can be incremented during SLEEP via external crystal/clock
- Timer2: 8-bit timer/counter with 8-bit period register, prescaler and postscaler
- Two Capture, Compare, PWM modules
  - Capture is 16-bit, max. resolution is 12.5 ns
  - Compare is 16-bit, max. resolution is 200 ns
  - PWM max. resolution is 10-bit
- 10-bit multi-channel Analog-to-Digital converter
- Synchronous Serial Port (SSP) with SPI™ (Master mode) and I^{2}C™ (Master/Slave)
- Universal Synchronous Asynchronous Receiver Transmitter (USART/SCI) with 9-bit address detection
- Parallel Slave Port (PSP) 8-bits wide, with external $\overline{RD}$, $\overline{WR}$ and $\overline{CS}$ controls (40/44-pin only)
- Brown-out detection circuitry for Brown-out Reset (BOR)

DS30292C-page 1

Figure B-1: Microchip PIC16F873 Microcontroller Data Sheet

PIC16F87X

Pin Diagrams

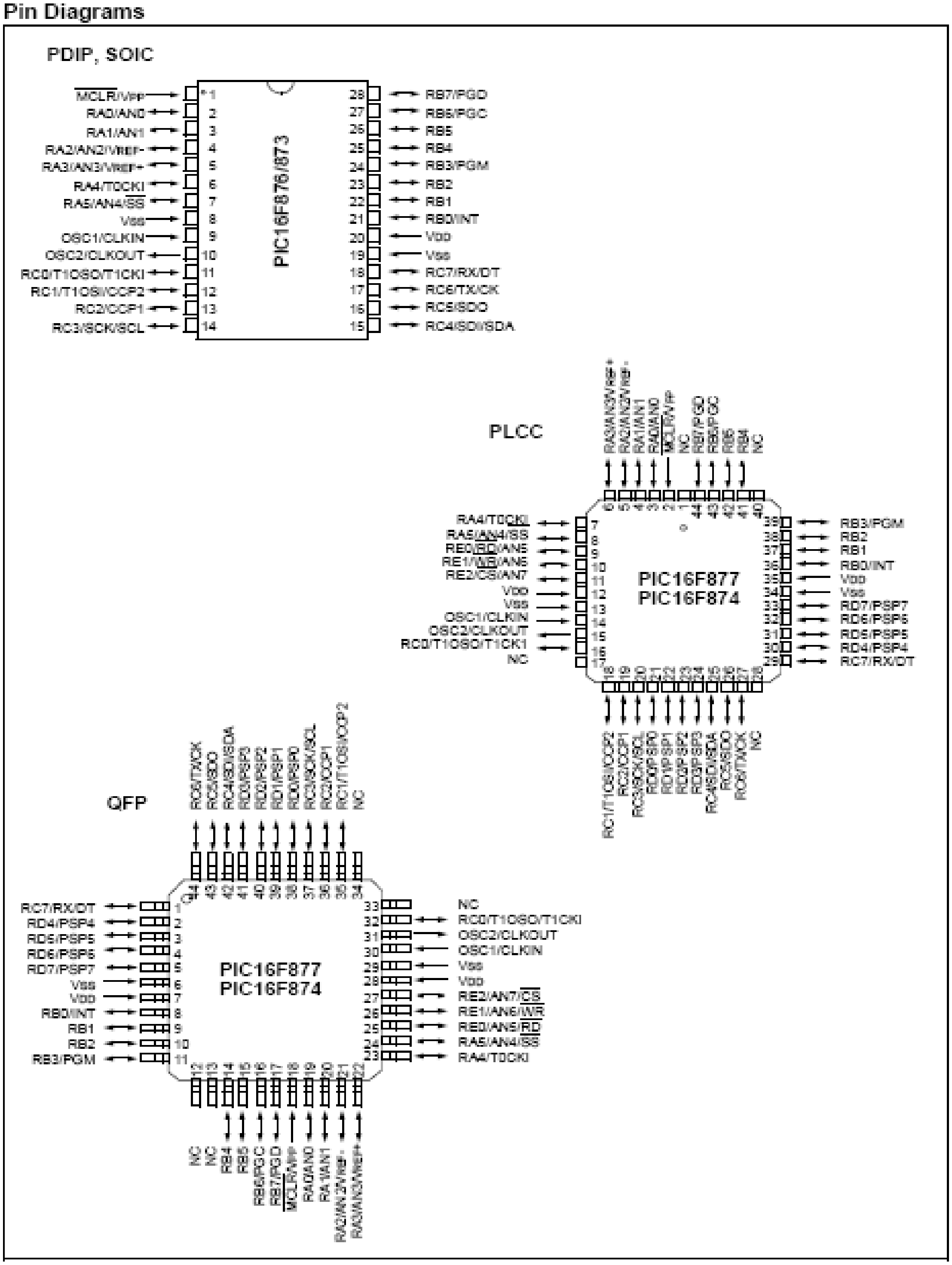

DS30292C-page 2

© 2001 Microchip Technology Inc.

Figure B-2(b): Microchip PIC16F873 Microcontroller Data Sheet

Key Features PICmicro™ Mid-Range Reference Manual (DS33023)	PIC16F873	PIC16F874	PIC16F876	PIC16F877
Operating Frequency	DC - 20 MHz	DC - 20 MHz	DC - 20 MHz	DC - 20 MHz
RESETS (and Delays)	POR, BOR (PWRT, OST)	POR, BOR (PWRT, OST)	POR, BOR (PWRT, OST)	POR, BOR (PWRT, OST)
FLASH Program Memory (14-bit words)	4K	4K	8K	8K
Data Memory (bytes)	192	192	368	368
EEPROM Data Memory	128	128	256	256
Interrupts	13	14	13	14
I/O Ports	Ports A,B,C	Ports A,B,C,D,E	Ports A,B,C	Ports A,B,C,D,E
Timers	3	3	3	3
Capture/Compare/PWM Modules	2	2	2	2
Serial Communications	MSSP, USART	MSSP, USART	MSSP, USART	MSSP, USART
Parallel Communications	—	PSP	—	PSP
10-bit Analog-to-Digital Module	5 input channels	8 input channels	5 input channels	8 input channels
Instruction Set	35 instructions	35 instructions	35 instructions	35 instructions

Figure B-3(c): Microchip PIC16F873 Microcontroller Data Sheet

APPENDIX C (Power MOSFET)

IRF150

Absolute Maximum Ratings $T_C = 25^oC$, Unless Otherwise Specified

		IRF150	UNITS
Drain to Source Voltage (Note 1)	V_{DS}	100	V
Drain to Gate Voltage ($R_{GS} = 20k\Omega$) (Note 1)	V_{DGR}	100	V
Continuous Drain Current	ID	40	A
$T_C = 100^oC$	I_D	25	A
Pulsed Drain Current (Note 3)	I_{DM}	160	A
Gate to Source Voltage	V_{GS}	±20	V
Maximum Power Dissipation	P_D	150	W
Linear Derating Factor		1.2	W/^{o}C
Single Pulse Avalanche Energy Rating (Note 4)	E_{AS}	150	mJ
Operating and Storage Temperature	T_J, T_{STG}	-55 to 150	^{o}C
Maximum Temperature for Soldering			
Leads at 0.063in (1.6mm) from Case for 10s	T_L	300	^{o}C
Package Body for 10s, See Techbrief 334	T_{pkg}	260	^{o}C

CAUTION: Stresses above those listed in "Absolute Maximum Ratings" may cause permanent damage to the device. This is a stress only rating and operation of the device at these or any other conditions above those indicated in the operational sections of this specification is not implied.

NOTE:

1. $T_J = 25^oC$ to 125^oC.

Electrical Specifications $T_C = 25^oC$, Unless Otherwise Specified

PARAMETER	SYMBOL	TEST CONDITIONS	MIN	TYP	MAX	UNITS
Drain to Source Breakdown Voltage	BV_{DSS}	$V_{GS} = 0V$, $I_D = 250\mu A$ (Figure 10)	100	-	-	V
Gate to Threshold Voltage	$V_{GS(TH)}$	$V_{GS} = V_{DS}$, $I_D = 250\mu A$	2.0	-	4.0	V
Zero Gate Voltage Drain Current	I_{DSS}	V_{DS} = Rated BV_{DSS}, $V_{GS} = 0V$	-	-	25	µA
		V_{DS} = 0.8 x Rated BV_{DSS}, $V_{GS} = 0V$, $T_J = 125^oC$	-	-	250	µA
On-State Drain Current (Note 2)	$I_{D(ON)}$	$V_{DS} > I_{D(ON)} \times r_{DS(ON)MAX}$, $V_{GS} = 10V$	40	-	-	A
Gate to Source Leakage Current	I_{GSS}	$V_{GS} = \pm 20V$	-	-	±100	nA
Drain to Source On Resistance (Note 2)	$r_{DS(ON)}$	$V_{GS} = 10V$, $I_D = 20A$ (Figures 8, 9)	-	0.045	0.055	Ω
Forward Transconductance (Note 2)	g_{fs}	$V_{DS} > I_{D(ON)} \times r_{DS(ON)MAX}$, $I_D = 20A$ (Figure 12)	9.0	11	-	S
Turn-On Delay Time	$t_{d(ON)}$	$V_{DD} = 24V$, $I_D \approx 20A$, $R_G = 4.7\Omega$, $R_L = 1.2\Omega$ (Figures 17, 18) MOSFET Switching Times are Essentially Independent of Operating Temperature	-	-	35	ns
Rise Time	t_r		-	-	100	ns
Turn-Off Delay Time	$t_{d(OFF)}$		-	-	125	ns
Fall Time	t_f		-	-	100	ns
Total Gate Charge (Gate to Source + Gate to Drain)	$Q_{g(TOT)}$	$V_{GS} = 10V$, $I_D = 50A$, V_{DS} = 0.8 x Rated BV_{DSS}, $I_{g(REF)} = -1.5mA$ (Figures 14, 19, 20) Gate Charge is Essentially Independent of Operating Temperature	-	63	120	nC
Gate to Source Charge	Q_{gs}		-	27	-	nC
Gate to Drain "Miller" Charge	Q_{gd}		-	36	-	nC
Input Capacitance	C_{ISS}	$V_{GS} = 0V$, $V_{DS} = 25V$, f = 1.0MHz (Figure 11)	-	2000	-	pF
Output Capacitance	C_{OSS}		-	1000	-	pF
Reverse Transfer Capacitance	C_{RSS}		-	350	-	pF
Internal Drain Inductance	L_D	Measured between the Contact Screw on the Flange that is Closer to Source and Gate Pins and the Center of Die / Modified MOSFET Symbol Showing the Internal Devices Inductances 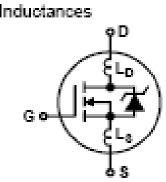	-	5.0	-	nH
Internal Source Inductance	L_S	Measured from the Source Lead, 6mm (0.25in) from the Flange and the Source Bonding Pad	-	12.5	-	nH
Thermal Impedance Junction to Case	$R_{\theta JC}$		-	-	0.8	^{o}C/W
Thermal Impedance Junction to Ambient	$R_{\theta JA}$	Free Air Operation	-	-	30	^{o}C/W

2 intersil

Figure C-1: Intersil IRF150 Power MOSFET Data Sheet

Source to Drain Diode Specifications

PARAMETER	SYMBOL	TEST CONDITIONS		MIN	TYP	MAX	UNITS
Continuous Source to DrainCurrent	I_{SD}	Modified MOSFET Symbol Showing the Integral Reverse P-N Junction Diode	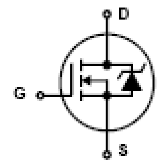	-	-	40	A
Pulse Source to Drain Current (Note 3)	I_{SDM}			-	-	160	A
Diode Source to Drain Voltage (Note 2)	V_{SD}	$T_J = 25^oC$, $I_{SD} = 40A$, $V_{GS} = 0V$ (Figure 13)		-	-	2.5	V
Reverse Recovery Time	t_{rr}	$T_J = 150^oC$, $I_{SD} = 40A$, $dI_{SD}/dt = 100A/\mu s$		-	600	-	ns
Reverse Recovery Charge	Q_{RR}	$T_J = 25^oC$, $I_{SD} = 5.5A$, $dI_{SD}/dt = 100A/\mu s$		-	3.3	-	μC

NOTES:

2. Pulse test: pulse width ≤ 300μs, duty cycle ≤ 2%.
3. Repetitive rating: pulse width limited by Max junction temperature. See Transient Thermal Impedance curve (Figure 3).
4. $V_{DD} = 10V$, starting $T_J = 25^oC$, $L = 170\mu H$, $R_G = 50\Omega$, Peak $I_{AS} = 40A$. See Figures 15, 16.

Typical Performance Curves Unless Otherwise Specified

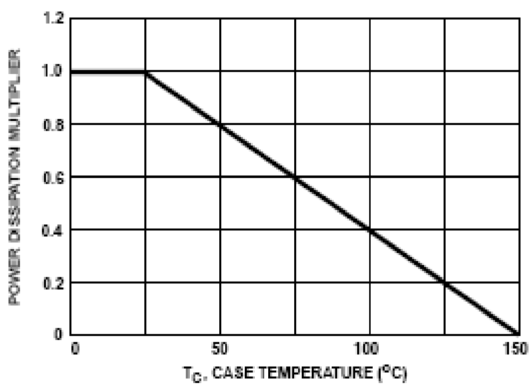

FIGURE 1. NORMALIZED POWER DISSIPATION vs CASE TEMPERATURE

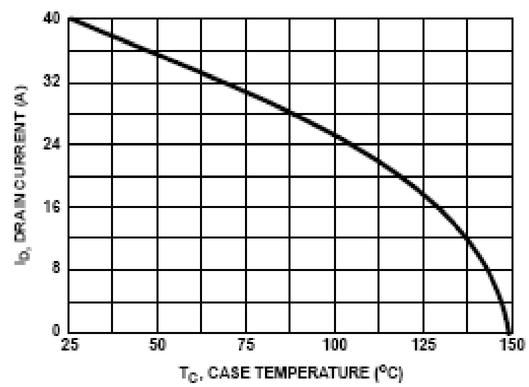

FIGURE 2. MAXIMUM CONTINUOUS DRAIN CURRENT vs CASE TEMPERATURE

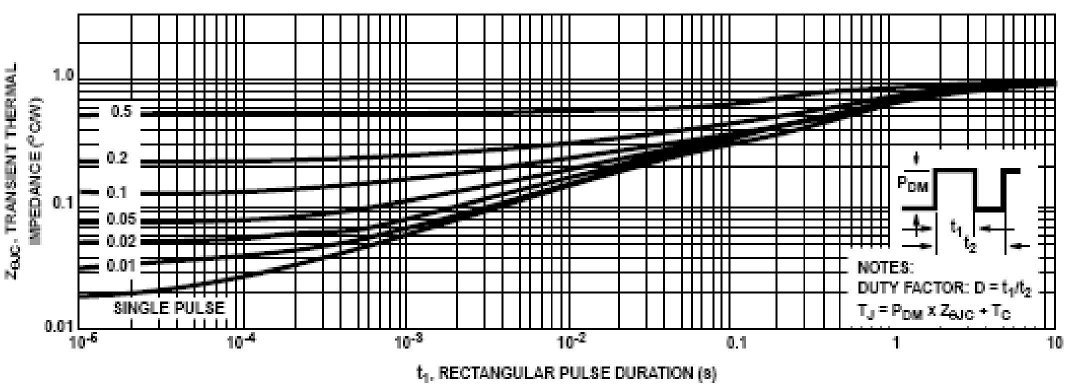

FIGURE 3. MAXIMUM TRANSIENT THERMAL IMPEDANCE

Figure C-1(b): Intersil IRF150 Power MOSFET Data Sheet

Typical Performance Curves Unless Otherwise Specified (Continued)

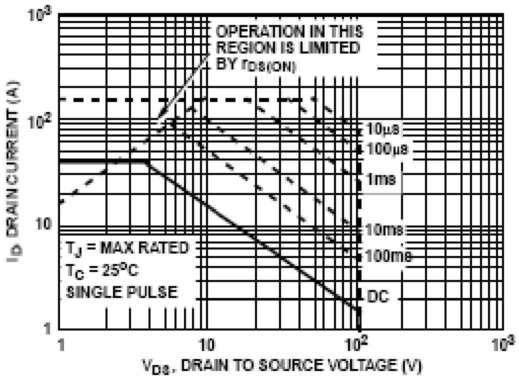

FIGURE 4. FORWARD BIAS SAFE OPERATING AREA

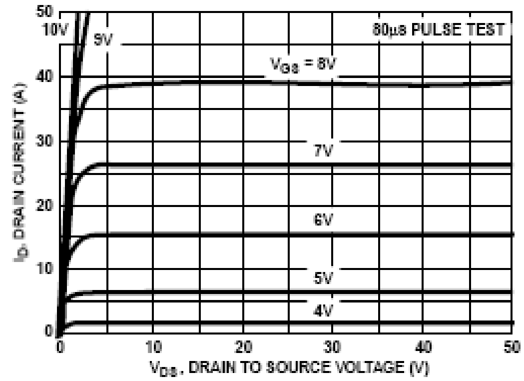

FIGURE 5. OUTPUT CHARACTERISTICS

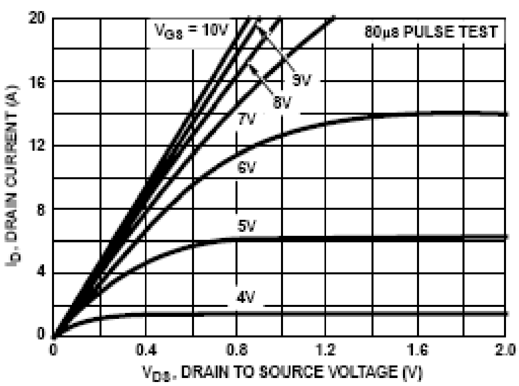

FIGURE 6. SATURATION CHARACTERISTICS

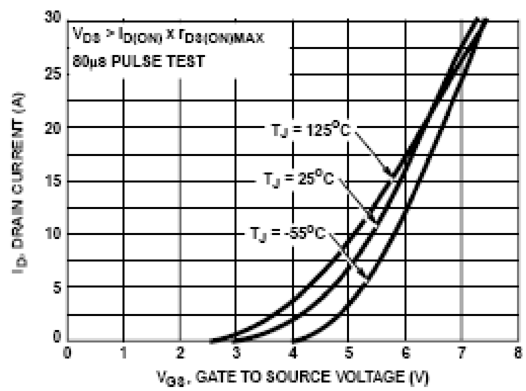

FIGURE 7. TRANSFER CHARACTERISTICS

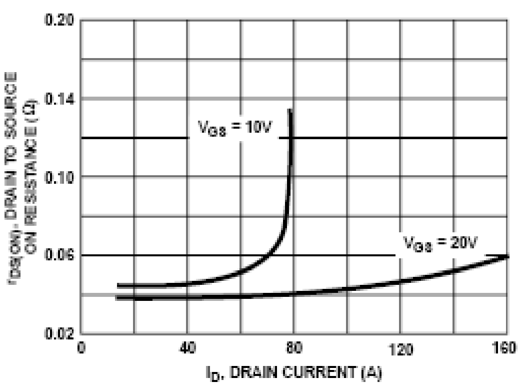

NOTE: Heating effect of 2μs is minimal.

FIGURE 8. DRAIN TO SOURCE ON RESISTANCE vs GATE VOLTAGE AND DRAIN CURRENT

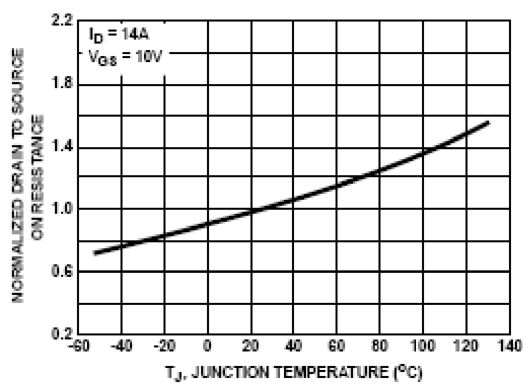

FIGURE 9. NORMALIZED DRAIN TO SOURCE ON RESISTANCE vs JUNCTION TEMPERATURE

Figure C-1(c): Intersil IRF150 Power MOSFET Data Sheet

Typical Performance Curves Unless Otherwise Specified (Continued)

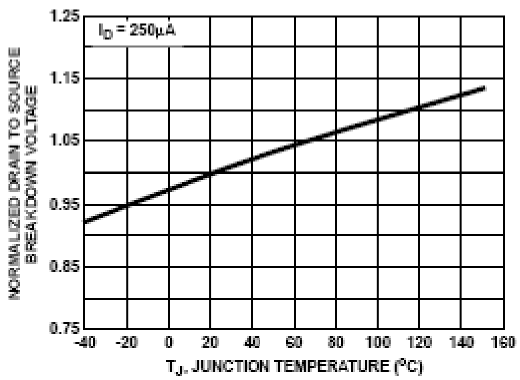

FIGURE 10. NORMALIZED DRAIN TO SOURCE BREAKDOWN VOLTAGE vs JUNCTION TEMPERATURE

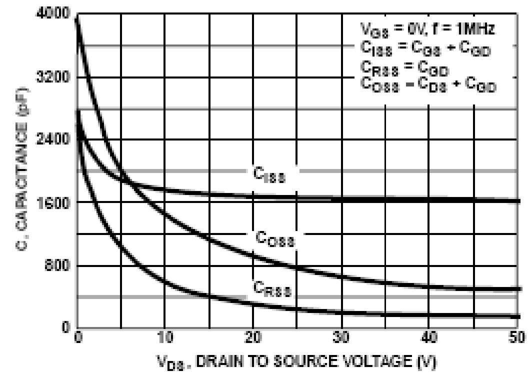

FIGURE 11. CAPACITANCE vs DRAIN TO SOURCE VOLTAGE

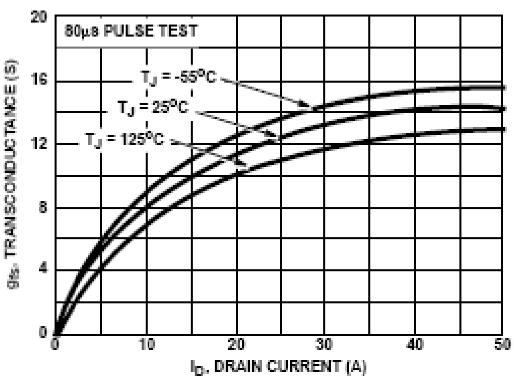

FIGURE 12. TRANSCONDUCTANCE vs DRAIN CURRENT

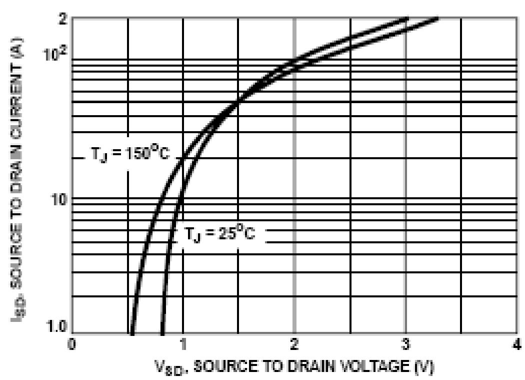

FIGURE 13. SOURCE TO DRAIN DIODE VOLTAGE

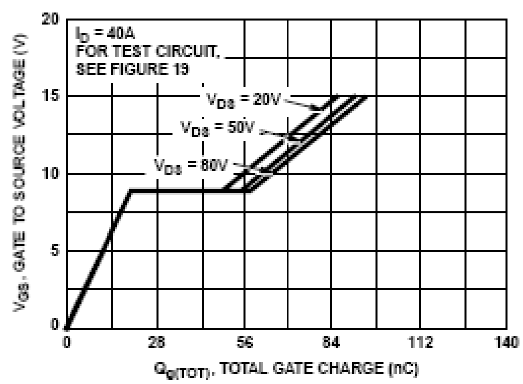

FIGURE 14. GATE TO SOURCE VOLTAGE vs GATE CHARGE

Figure C-1(d): Intersil IRF150 Power MOSFET Data Sheet

Test Circuits and Waveforms

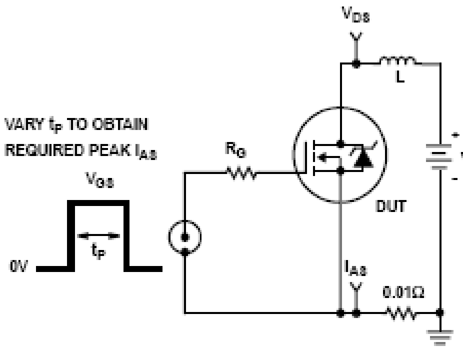

FIGURE 15. UNCLAMPED ENERGY TEST CIRCUIT

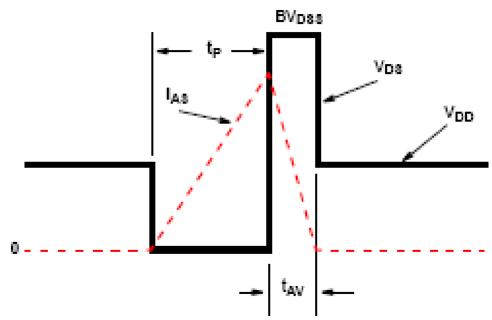

FIGURE 16. UNCLAMPED ENERGY WAVEFORMS

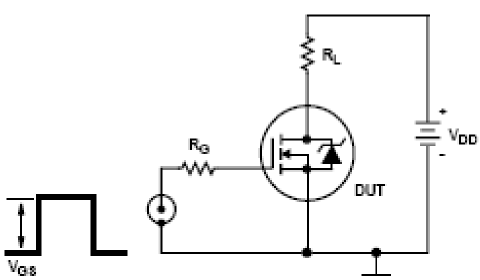

FIGURE 17. SWITCHING TIME TEST CIRCUIT

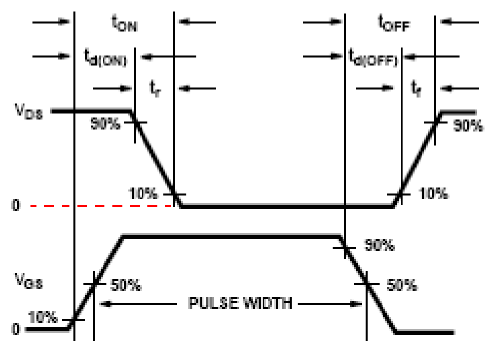

FIGURE 18. RESISTIVE SWITCHING WAVEFORMS

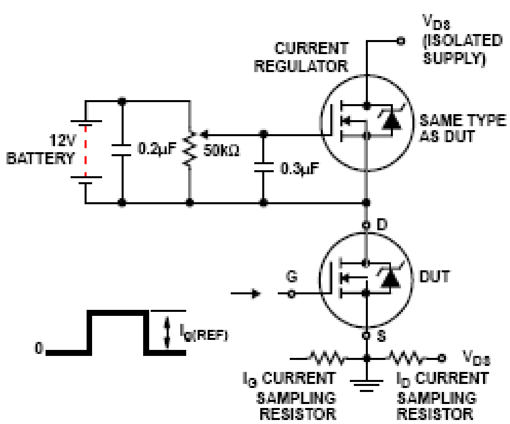

FIGURE 19. GATE CHARGE TEST CIRCUIT

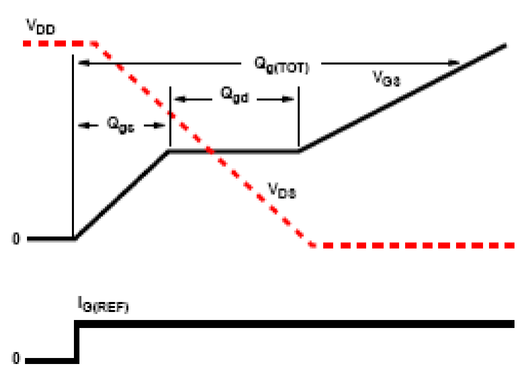

FIGURE 20. GATE CHARGE WAVEFORMS

Figure C-1(e): Intersil IRF150 Power MOSFET Data Sheet

APPENDIX D (Schottky Diode)

MBR0520L

FAIRCHILD
SEMICONDUCTOR®

MBR0520L

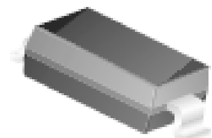

Features

- 0.5 Ampere, low forward voltage, less then 385mV
- 400 milliwatt Power Dissipation package
- Compact surface mount package with the same footprint as mini-melf

SOD123
Color Band Denotes Cathode
Mark: B2

Schottky Rectifier

Absolute Maximum Ratings* T_A = 25°C unless otherwise noted

Symbol	Parameter	Value	Units
V_{RRM}	Maximum Repetitive Reverse Voltage	20	V
$I_{F(AV)}$	Average Rectified Forward Current	500	mA
I_{FSM}	Non Repetitive Peak Forward Current (Surge applied at rated load conditions half wave, single phase, 60 Hz)	5.5	A
T_{stg}	Storage Temperature Range	-65 to +150	°C
$T_{J\,max}$	Operating Junction Temperature	-65 to +125	°C

*These ratings are limiting values above which the serviceability of any semiconductor device may be impaired.

Thermal Characteristics

Symbol	Parameter	Value	Units
$R_{\theta JA}$	Thermal Resistance Junction to Ambient*	340	°C/W
$R_{\theta JL}$	Thermal Resistance Junction to Lead	150	°C/W

*FR-4 or FR-5 = 3.5 x 1.5 inches using minimum recommended Land Pads.

Electrical Characteristics T_A = 25°C unless otherwise noted

Symbol	Parameter		Value	Units
V_F	Forward Voltage	@ I_F = 100 mA,	300	mV
		I_F = 100 mA, T_A = 100 °C	220	mV
		I_F = 500 mA,	385	mV
		I_F = 500 mA, T_A = 100 °C	330	mV
I_R	Reverse Current	@ V_R = 10 V,	75	µA
		V_R = 10 V, T_A = 100 °C	5.0	mA
		V_R = 20 V,	250	µA
		V_R = 20 V, T_A = 100 °C	8.0	mA

MBR0520L, Rev. B

Figure D-1: Fairchild Semiconductor MBR0520L Schottky Diode Data Sheet

MBR0520L

Schottky Rectifier
(continued)

Typical Characteristics

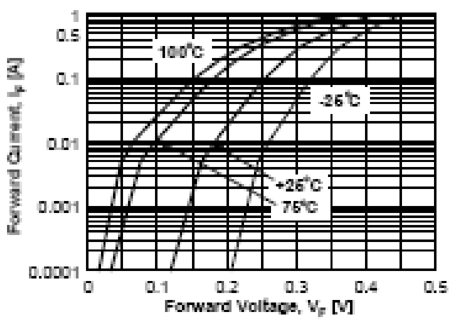

Figure 1. Forward Voltage Characteristics

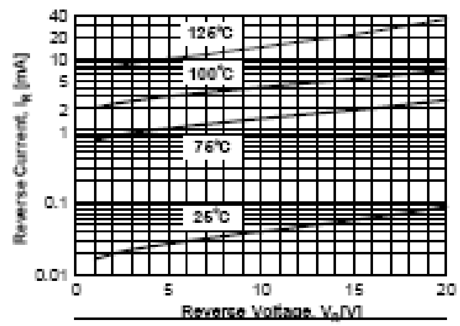

Figure 2. Reverse Current vs Reverse Voltage

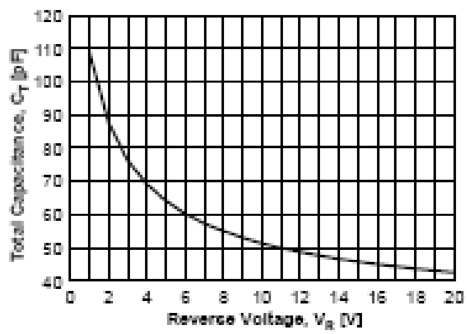

Figure 3. Total Capacitance

MBR0520L, Rev. B

Figure D-2: Fairchild Semiconductor MBR0520L Schottky Diode Data Sheet

APPENDIX E (Current Sensor)

Current Transducer LA 03 .. 20-PB

I_{PN} = 3 .. 20 A

For the electronic measurement of currents: DC, AC, pulsed, mixed, with a galvanic isolation between the primary circuit (high power) and the secondary circuit (electronic circuit).

Preliminary

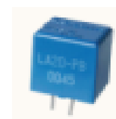

Electrical data

Primary nominal current (A)	Primary nominal r.m.s. current I_{PN} (A)	Primary current measuring range I_P (A)	Primary Conductor Diameter (mm)	Type
3	3	± 4.5	0.5	LA 03-PB
5	3	± 7.5	0.5	LA 06-PB
10	5	± 15	0.65	LA 10-PB
15	7.5	± 22.5	0.8	LA 16-PB
20	10	± 30	1.0	LA 20-PB

V_C	Supply voltage (± 5 %)	± 15	V
I_C	Current consumption	app. 20mA+ I_{PN}/1200	mA
V_d	R.m.s. voltage for AC isolation test, 50/60Hz,1mn	2.5	kV
R_{IS}	Isolation resistance @ 500 VDC	> 500	MΩ
V_{OUT}	Output voltage @ ± I_{PN}, R_L = 10 kΩ, T_A = 25°C	± 4	V
R_L	Load resistance	> 10	kΩ

Accuracy-Dynamic performance data

X	Accuracy @ I_{PN}, T_A = 25°C (without offset)	< ± 1.5 % of I_{PN}	
ε_L	Linearity (0 .. ± I_{PN})	< ± 1 % of I_{PN}	
V_{OE}	Electrical offset voltage, T_A = 25°C	< ± 30	mV
V_{OH}	Hysteresis offset voltage @ I_P = 0; after an excursion of 1 x I_{PN}	< ± 15	mV
V_{OT}	Thermal drift of V_{OE} max.	± 1	mV/K
$TC\varepsilon_G$	Thermal drift(% of reading)	< 0.04	%/K
t_r	Response time @ 90% of I_P	< 3	µs
f	Frequency bandwidth (- 1dB)[2]	DC .. 150	kHz

General data

T_A	Ambient operating temperature	- 10 .. + 80	°C
T_S	Ambient storage temperature	- 15 .. + 85	°C
m	Mass	< 12	g

Notes : EN 50178 approval pending
[1] Calibration for 4V output is carried out at the primary normal current.
[2] Derating is needed to avoid excessive core heating at high frequency.

Features

- Closed loop (compensation) current transducer using the Hall effect
- Voltage output
- Printed circuit board mounting

Advantages

- Excellent accuracy
- Very good linearity
- Low temperature drift
- Optimized response time
- Wide frequency bandwidth
- No insertion losses
- High immunity to external interference
- Current overload capacity

Applications

- AC variable speed drives and servo motor drives
- Static converters for DC motor drives
- Battery supplied applications
- Uninterruptible Power Supplies (UPS)
- Switched Mode Power Supplies (SMPS)
- Switched Mode Power Supplies (SMPS)
- Power supplies for welding applications

010809/3

LEM Components www.lem.com

Figure E-1: LEM LA-10PB Current Sensor Data Sheet

LA 03 ... 20-PB

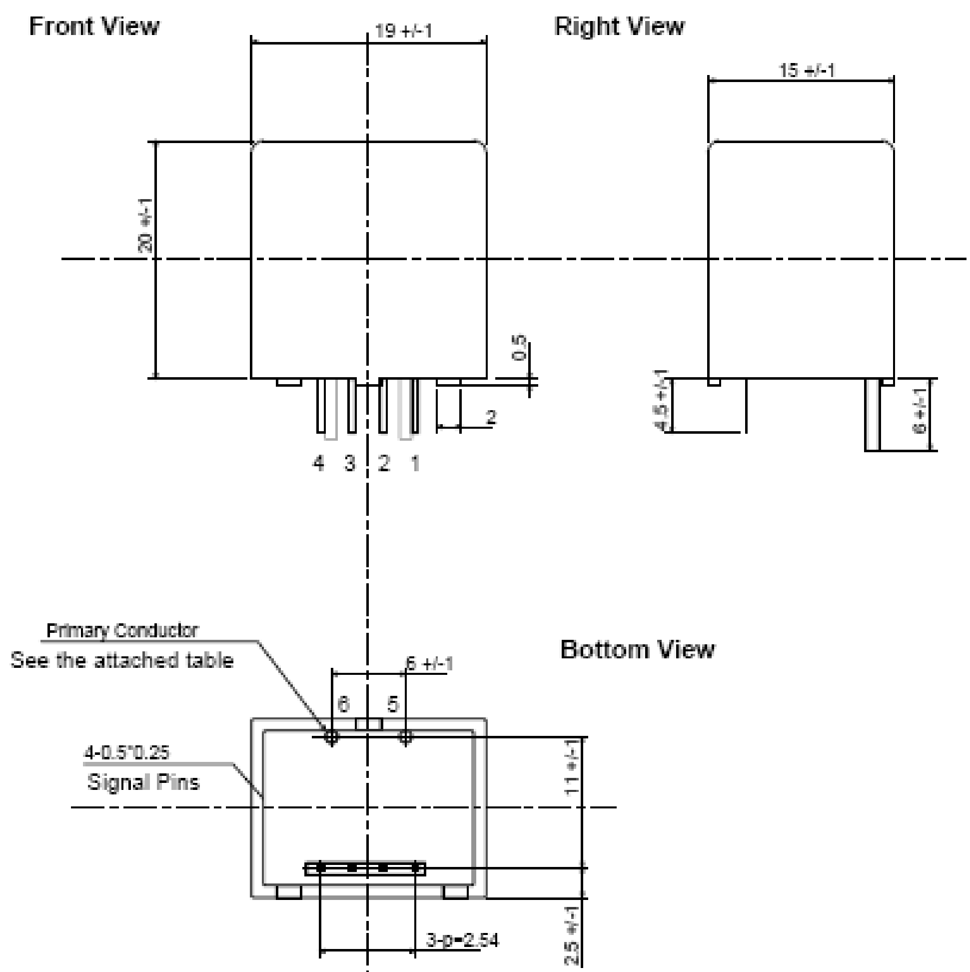

Terminal Pin Identification

Primary Conductor

Part No.	Diameter
LA 03PB	0.5 d
LA 05PB	0.5 d
LA 10PB	0.65 d
LA 15PB	0.8 d
LA 20PB	1.0 d

Signal Pins

1	-Vcc
2	0V
3	+Vcc
4	Output

Direction of Current Flow

5 (+) ⟶ 6 (-)

UNIT : mm

Figure E-1(b): LEM LA-10PB Current Sensor Data Sheet

REFERENCES

1. Scott, W.G., "Distributed Power Generation: Planning and Evaluation," Marcel Dekker, 2000.

2. Coutts, T.J., Fitzgerald, M.C., "Thermophotovoltaics," Scientific American Magazine, pp.90-95, September 1998.

3. Yablonovitch, E., "Photonic Band-gap Structures," Journal of the Optical Society of America B, 10:283, 1993.

4. Luque, A., Marti, A., "Increasing the Efficiency of Ideal Solar Cells by Photon Induced Transitions at Intermediate Levels," Physical Review Letters, 78(26): 5014-5017, June 1997.

5. Antunes, F.L.M., Santos, J.L., "Maximum Power Point Tracker for PV Systems," World Climate & Energy Event, December 2003.

6. Neville, R. C., "Solar Energy Conversion," Elsevier Science, 1995.

7. Niemann, J., "Understanding Solar Cell Physics," Sensors, 21(5):57–62, May 2004.

8. Cope, R.C., Podrazhansky, Y., "The Art of Battery Charging," Battery Conference on Applications and Advances, 14:233-235, January, 1999.

9. Castaner, L., Silvestre, S., "Modeling Photovoltaic Systems," Wiley, 2002.

10. Costamagna, P., Srinivasan, S., "Quantum Jumps in the PEMFC Science and Technology from the 1960s to the Year 2000," Journal of Power Sources, 102:242-252, 2001.

11. IDATECH, "IFCS 1200 Brochure," www.idatech.com.

12. Barker, P.P., "Ultracapacitors for Use in Power Quality and Distributed Resource Applications," Power Engineering Society Summer Meeting, 1:316-320.

13. Enslin, J.H.R., Swiegers, W., "An Integrated Maximum Power Point Tracker for Photovoltaic Panels," IEEE International Symposium on Industrial Electronics, 1:40-44, July 1998.

14. Bloos, H., et al., "Photovoltaic Pumping Systems," EuroSun96, pp.583-589, 1996.

15. Chung, H.S.H., Ho, M.T., Hui, S.Y.R., Tse, K.K., "A Novel Maximum Power Point Tracking Technique for PV Panels," Power Electronics Specialist Conference, 4:1970-1975, June 2001.

16. Forsyth, A.J., Mollov, S.V., "Modelling and Control of DC-DC Converters," Power Engineering Journal, 12(5):229-236, October 1998.

17. Walker, G., "Evaluating MPPT Converter Topologies Using a MATLAB PV Model," Journal of Electrical and Electronic Engineering, 21:49-56, 2001.

18. Arabi, K., Kaminska, B., "Testing Analog and Mixed-Signal Integrated Circuits Using Oscillation-Test Method," IEEE Trans. Computer-Aided Design of Integrated Circuits and Systems, 16(7):745-753, July 1997.

19. Alonso C., et al., "MPPT of Photovoltaic Systems Using Extremum-Seeking Control," 42(1):249-258, January 2006.

20. Baliga, B.J., "Power Semiconductor Device Figure of Merit for High-Frequency Applications," IEEE Electron Device Letters, 10(10):455-457, October 1989.

21. Erickson, R.W., Maksimovic, D., "Fundamentals of Power Electronics," Springer, 2001.

22. Barrass, P., Cade, M., "PWM Rectifier Using Indirect Voltage Sensing," IEE Proceedings on Electric Power Applications, 146(5):539-544, September 1999.

23. Chimento, G., et al., "Effects of Irradiance and Other Factors on PV Temperature Coefficients," IEEE Record of Photovoltaic Specialists Conference, 1:608-613, October 1991.

24. Ernest van Dyk, E., Meyer, E.L., "The Effect of Reduced Shunt Resistance and Shading on Photovoltaic Module Performance," IEEE Record of Photovoltaic Specialists Conference, pp.1331-1334, January 2005.

25. Parretta, A., Sarno, A., Vicari, L.R.M., "Effects of Solar Irradiation Conditions on the Outdoor Performance of Photovoltaic Modules," Optics Communication, 153(1):153-156, July 1998.

26. Chung, H.S.H., Ho, M.T., Hui, S.Y.R., Tse, K.K., "A Comparative Study of Maximum-Power-Point Trackers for Photovoltaic Panels Using Switching-Frequency Modulation Scheme," IEEE Trans. Industrial Electronics, 51(2):410-418, April 2004.

27. Chihchiang, H., Chihming, S., "Study of Maximum Power Tracking Techniques and Control of DC/DC Converters for Photovoltaic Power System," IEEE Record of Power Electronics Specialists Conference, pp.86-93, 1998.

28. Abdul-Latif, M., Sayuti, S.H., Wanik, M.Z., Yusof, Y., "Modeling and Simulation of Maximum Power Point Tracker for Photovoltaic System," Proceedings on Power and Energy Conference, pp.88-936, November 2004.

29. Chihchiang H., Chihming S., Jongrong L., “Implementation of a DSP-Controlled Photovoltaic System with Peak Power Tracking,” IEEE Trans. Industrial Electronics, 45(1):99-107, February 1998.

30. Liu, X., Lopes, L.A.C., “An Improved Perturbation and Observation Maximum Power Point Tracking Algorithm for PV Arrays,” Power Electronics Specialists Conference, 3:2005-2010, June 2004.

31. Fernia, N., Petrone, G., Spagnuolo, G., Vitelli, M., “Optimizing Duty-Cycle Perturbation of P&O MPPT Technique,” Power Electronics Specialists Conference, 3:1939-1944, June 2004.

32. Premrudeepreechacharn, S., Patanapirom, N., “Solar-Array Modelling and Maximum Power Point Tracking Using Neural Networks,” IEEE Bologna Power Technology Conference, Italy, June 2003.

33. Hassoun, M.H., “Fundamentals of Artificial Neural Networks,” Proceedings of the IEEE, 84(6):906, June 1996.

34. Senjyu, T., Veerachary, M., Uezato, K., “Feedforward Maximum Power Point Tracking of PV Systems Using Fuzzy Controller,” IEEE Trans. Aerospace and Electronic Systems, 38(3):969-981, July 2002.

35. Piche, S.W., “Steepest Descent Algorithms for Neural Network Controllers and Filters,” IEEE Trans. Neural Networks, 5(2):198-212, March 1994.

BIOGRAPHICAL SKETCH

Adedamola Omole was born and raised in Ile-Ife, Osun State, Nigeria. He attended high school at Federal Government College, Odogbolu and obtained his B.S. degree in Electrical Engineering from Florida State University in 2004. He joined the M.S. program at FSU in 2004 and worked under the supervision of Dr. Jie Chang at the Center for Advanced Power System (CAPS). Damola is a member of IEEE and his area of interest include power and communication systems.